Petrological traverse of the olivine cumulate Séítah formation at Jezero crater, Mars : A perspective from SuperCam onboard Perseverance

O. Beyssac, O. Forni, A. Cousin, A. Udry, L.C. Kah, L. Mandon, E. Clavé, Y. Liu, F. Poulet, C. Quantin Nataf, et al.

To cite this version:

O. Beyssac, O. Forni, A. Cousin, A. Udry, L.C. Kah, et al.. Petrological traverse of the olivine cumulate Séítah formation at Jezero crater, Mars : A perspective from SuperCam onboard Perseverance. Journal of Geophysical Research. Planets, 2023, The MARS Perseverance Rover Jezero Crater Floor Campaign, 128 (7), pp.e2022JE007638. 10.1029/2022JE007638 . insu-04116300

HAL Id: insu-04116300
https://insu.hal.science/insu-04116300v1

Submitted on 1 Nov 2023

JGR Planets

RESEARCH ARTICLE
10.1029/2022JE007638

Special Section:
The Mars Perseverance Rover Jezero Crater Floor Campaign

Key Points:

- The Séítah formation consists of an olivine cumulate series, weakly altered, preserving the igneous texture and mineralogy
- Emplacement of the Séítah formation required fractional crystallization and slow cooling of the parent magma at depth and erosion
- The Séítah formation could be a particular member of the Nili Fossae regional olivine-carbonate unit observed from orbit

Supporting Information:

Supporting Information may be found in the online version of this article.

Correspondence to:

O. Beyssac,
Olivier.Beyssac@upmc.fr

Citation:

Beyssac, O., Forni, O., Cousin, A., Udry, A., Kah, L. C., Mandon, L., et al. (2023). Petrological traverse of the olivine cumulate Séítah formation at Jezero crater, Mars: A perspective from SuperCam onboard Perseverance. *Journal of Geophysical Research: Planets*, *128*, e2022JE007638. https://doi.org/10.1029/2022JE007638

Received 25 OCT 2022
Accepted 17 MAY 2023

Petrological Traverse of the Olivine Cumulate Séítah Formation at Jezero Crater, Mars: A Perspective From SuperCam Onboard Perseverance

O. Beyssac[1], O. Forni[2], A. Cousin[2], A. Udry[3], L. C. Kah[4], L. Mandon[5], O. E. Clavé[6], Y. Liu[7], F. Poulet[8], C. Quantin Nataf[9], O. Gasnault[2], J. R. Johnson[10], K. Benzerara[1], P. Beck[11], E. Dehouck[9], N. Mangold[12], C. Alvarez Llamas[13], R. B. Anderson[14], G. Arana[15], R. Barnes[16], S. Bernard[1], T. Bosak[17], A. J. Brown[18], K. Castro[15], B. Chide[19], S. M. Clegg[19], E. Cloutis[20], T. Fouchet[5], T. Gabriel[14], S. Gupta[16], G. Lacombe[2,21], J. Lasue[2], S. Le Mouelic[12], G. Lopez-Reyes[22], J. M. Madariaga[15], F. M. McCubbin[23], S. M. McLennan[24], J. A. Manrique[2,22], P. Y. Meslin[2], F. Montmessin[21], J. Núñez[10], A. M. Ollila[19], A. Ostwald[3], P. Pilleri[2], P. Pinet[2], C. Royer[5], S. K. Sharma[25], S. Schröder[26], J. I. Simon[27], M. J. Toplis[2], M. Veneranda[22], P. A. Willis[7], S. Maurice[2], R. C. Wiens[28], and The SuperCam Team[29]

[1]Institut de Minéralogie, de Physique des Matériaux et de Cosmochimie, CNRS UMR 7590, Sorbonne Université, Muséum National d'Histoire Naturelle, Paris, France, [2]Institut de Recherche en Astrophysique et Planétologie, Université de Toulouse 3 Paul Sabatier, CNRS, CNES, Toulouse, France, [3]Department of Geoscience, University of Nevada, Las Vegas, Las Vegas, NV, USA, [4]Department of Earth and Planetary Sciences, University of Tennessee, Knoxville, Knoxville, TN, USA, [5]Laboratoire d'Etudes Spatiales et d'Instrumentation en Astrophysique, Observatoire de Paris-PSL, CNRS, Sorbonne Université, Université de Paris Cité, Meudon, France, [6]Centre Lasers Intenses et Applications, CNRS, CEA, Université de Bordeaux, Bordeaux, France, [7]Jet Propulsion Laboratory, California Institute of Technology, Pasadena, CA, USA, [8]Institut d'Astrophysique Spatiale, CNRS, Université Paris-Saclay, Orsay, France, [9]Laboratoire de Géologie de Lyon: Terre, Université de Lyon, Université Claude Bernard Lyon1, Ecole Normale Supérieure de Lyon, Université Jean Monnet Saint Etienne, CNRS, Villeurbanne, France, [10]Space Exploration Sector, Johns Hopkins University Applied Physics Laboratory, Laurel, MD, USA, [11]Institut de Planétologie et Astrophysique de Grenoble, CNRS, Université Grenoble Alpes, Grenoble, France, [12]Laboratoire de Planétologie et Géosciences, CNRS, Nantes Université, Université Angers, Nantes, France, [13]Department of Analytical Chemistry, University of Malaga (UMA), Malaga, Spain, [14]USGS Astrogeology Science Center, U.S. Geological Survey, Flagstaff, AZ, USA, [15]Department of Analytical Chemistry, University of the Basque Country, UPV/EHU, Leioa, Spain, [16]Department of Earth Sciences and Engineering, Imperial College London, London, UK, [17]Department of Earth, Atmospheric and Planetary Sciences, Massachusetts Institute of Technology, Cambridge, MA, USA, [18]Plancius Research, Severna Park, MD, USA, [19]Space and Planetary Exploration Team, Los Alamos National Laboratory, Los Alamos, NM, USA, [20]C-TAPE, University of Winnipeg, Winnipeg, MB, Canada, [21]Laboratoire Atmosphères, Milieux, Observations Spatiales, CNRS, Université Saint-Quentin-en-Yvelines, Université Paris Saclay, Sorbonne Université, Guyancourt, France, [22]Research Group ERICA, Universidad de Valladolid (UVa), Valladolid, Spain, [23]Astromaterials Research and Exploration Science, NASA Johnson Space Center, Houston, TX, USA, [24]Department of Geosciences, Stony Brook University, State University of New York, Stony Brook, NY, USA, [25]Hawai'i Institute of Geophysics and Planetology, University of Hawai'i at Mānoa, Honolulu, HI, USA, [26]Deutsches Zentrum fur Luft- und Raumfahrt (DLR), Institute of Optical Sensor Systems, Berlin, Germany, [27]Center for Isotope Cosmochemistry and Geochronology, Astromaterials Research and Exploration Science Division, NASA Johnson Space Center, Houston, TX, USA, [28]Department of Earth, Atmospheric, and Planetary Sciences, Purdue University, West Lafayette, IN, USA, [29]See Supporting Information S1

Abstract Séítah is the stratigraphically lowest formation visited by Perseverance in the Jezero crater floor. We present the data obtained by SuperCam: texture by imagery, chemistry by Laser-Induced Breakdown Spectroscopy, and mineralogy by Supercam Visible and Infrared reflectance and Raman spectroscopy. The Séítah formation consists of igneous, weakly altered rocks dominated by millimeter-sized grains of olivine with the presence of low-Ca and high-Ca pyroxenes, and other primary minerals (e.g., plagioclase, Cr-Fe-Ti oxides, phosphates). Along a ∼140 m long section in Séítah, SuperCam analyses showed evidence of geochemical and mineralogical variations, from the contact with the overlying Máaz formation, going deeper in the formation. Bulk rock and olivine Mg#, grain size, olivine content increase gradually further from the contact. Along the section, olivine Mg# is not in equilibrium with the bulk rock Mg#, indicating local olivine accumulation. These observations are consistent with Séítah being the deep ultramafic member of a cumulate series derived from the fractional crystallization and slow cooling of the parent magma at depth. Possible magmatic processes and exhumation mechanisms of Séítah are discussed. Séítah rocks show some affinity with some rocks at Gusev crater, and with some Martian meteorites suggesting that such rocks are not rare on the surface of Mars.

Séítah is part of the Nili Fossae regional olivine-carbonate unit observed from orbit. Future exploration of Perseverance on the rim and outside of the crater will help determine if the observations from the crater floor can be extrapolated to the whole unit or if this unit is composed of distinct sub-units with various origins.

Plain Language Summary The Mars 2020 Perseverance rover landed on Mars in the Jezero crater on 18 February 2021. An important goal of this mission is to constrain the geology of the Jezero crater and its delta, and to sample rocks to return to Earth. Here, we study the deepest rock formation observed close to the landing site on the crater floor, named the Séitah formation. We conclude that this formation is igneous with rocks consisting in the accumulation of dominant millimeter-sized olivine crystals with pyroxenes and other minerals. Such rocks form at depth by slow cooling of the magma, and the first mineral to crystallize (olivine) settles down by gravity in the magma. Such rocks bear similarity to other Martian rocks found in the Gusev crater by the Opportunity rover, and also to some Martian meteorites. These rocks will be studied in Earth-based laboratories and will allow us to better understand magmatic processes on Mars.

1. Introduction

The NASA Perseverance rover landed on 18 February 2021 at the "Octavia E. Butler" site, on the floor of Jezero crater in the Nili Fossae region of Mars. This landing site was selected as it shows compelling evidence for fluvial sedimentary deposits including ancient deltas identified from orbit (Fassett & Head, 2005). This site was also considered as an outstanding place for the astrobiological priority of the Mars2020 mission (Farley et al., 2020, 2022). During the first months of the mission, investigations by the Perseverance science team have confirmed that Jezero crater hosted a transient ancient lake system around the late Noachian to Early Hesperian transition, followed by a period of high energy detrital flows (Mangold et al., 2021). However, Jezero crater was also selected as it contains outcrops of the largest regional unit where olivine and carbonate have been detected on Mars based on Visible and Near Infrared spectroscopy from orbit, the Nili Fossae olivine-carbonate unit (Brown et al., 2020; Hoefen et al., 2003; Horgan et al., 2020; Mandon et al., 2020; Mustard et al., 2005). The presence of olivine is key to understanding magmatic petrology and planetary evolution, and its association with carbonate and clay phases suggests that fluid-rock interaction may have occurred locally. Such alteration environments have been considered as a possible niche for initiating, hosting, and preserving life on early Mars, as well as a good target to investigate Martian geochemical cycles involving water and carbon, and in turn, the geological and geochronological history of Mars (e.g., Farley et al., 2022 and references therein).

During the first year of the mission, Perseverance explored two important formations of the Jezero crater floor identified from orbit: Máaz (*Mars* in Navajo language) and Séítah (*Among the sands* in Navajo language), as informally named by the Perseverance team (Farley et al., 2022; Sun et al., 2023). Perseverance has several cameras onboard and conducts routine imaging along its traverse, from high-resolution images of rocks and outcrops in the vicinity of the rover to long-distance (up to tens of km) images of targets of interest (J. F. Bell et al., 2022; Maurice et al., 2021; Wiens et al., 2021). Perseverance also carries a comprehensive scientific payload allowing (a) remote analysis of rock chemistry and mineralogy, that is, from adjacent to the rover to long distances at several kilometers via SuperCam (Maurice et al., 2021; Wiens et al., 2021) and MastCam-Z (J. F. Bell et al., 2021, 2022), as well as (b) proximity Science, that is, chemical and mineralogical analysis at high spatial resolution in close proximity (2.5–4 cm) with a target by the Planetary Instrument for X-ray Lithochemistry (PIXL, Allwood et al., 2020), and Scanning Habitable Environments with Raman and Luminescence for Organics and Chemicals (SHERLOC, Bhartia et al., 2021) instruments. Remote Science has often been performed along the traverse, yielding a large data set that documents chemical and mineralogical variation of both local rocks and regolith (J. F. Bell et al., 2022; Wiens et al., 2022). Proximity Science has focused primarily on a few abraded patches (three in Séitah, four in Máaz) of about 5 cm diameter, where the surfaces of rocks were mechanically abraded by the rover to expose a flat and "fresh" surface (Farley et al., 2022; Liu et al., 2022). In addition to these instruments, Perseverance is also equipped with the Radar Imager for Mars Subsurface Experiment (RIMFAX) to image the structure of the first meters of the subsurface along the rover traverse (Hamran et al., 2022). Together, these instruments provide a complementary data set documenting the chemistry and mineralogy of the crater floor rocks from the sub-millimeter to the outcrop scale and, beyond, up to the scale of the formations (Farley et al., 2022; Sun et al., 2023).

This article focuses on the SuperCam data obtained on the rocks from the Séítah formation with an emphasis on the primary magmatic mineralogy. Similar investigations on the primary mineralogy of the Máaz formation using SuperCam data are presented by Udry et al. (2022), and the secondary alteration phases as seen from SuperCam for both formations are described in other papers (Clavé et al., 2022; Wiens et al., 2022). The specific use of Supercam Visible and Infrared reflectance (VISIR) spectroscopy to investigate mineralogy in Jezero crater was addressed by Mandon et al. (2022). SuperCam is a remote-sensing instrument that provides chemical and mineralogical information from targets, generally within 6.5 m of the rover, at a sub-mm to mm scale by combining Laser-Induced Breakdown Spectroscopy (LIBS), Raman and luminescence spectroscopy, and VISIR spectroscopy. SuperCam also includes a remote micro-imager (RMI) providing high-resolution context color images of the targets as well as a microphone. Microphone data are not discussed in this article, although it provides information about rock hardness (Chide et al., 2019, 2020). In addition to their capability to probe targets near the rover, SuperCam's passive techniques (VISIR spectroscopy and RMI imaging) can also operate effectively on targets at distances up to several kilometers. SuperCam LIBS provides a quantitative estimate of major elements (Anderson et al., 2022) present in the fraction of rock ablated by the laser within a ∼160–450 μm wide spot (Maurice et al., 2021), as well as detection and qualitative information on many light and/or minor elements (Maurice et al., 2021; Wiens et al., 2021). SuperCam LIBS has been frequently used (e.g., 225 targets up to sol 420), providing a geochemical profile of the Máaz and Séítah formations visited by Perseverance (Wiens et al., 2022), but also direct mineralogical information locally where grains were larger than the LIBS spot size. SuperCam has been instrumental in revealing the different bulk chemistry and mineralogy of these two formations: Máaz is basaltic to basaltic-andesite, Fe-rich, dominated by pyroxene and plagioclase (Udry et al., 2022; Wiens et al., 2022), while Séítah is mafic to ultramafic, Mg-rich, and dominated by olivine and pyroxene (Wiens et al., 2022; this study). First year investigations have demonstrated that both formations are clearly igneous and weakly altered (Farley et al., 2022; Liu et al., 2022; Sun et al., 2023; Wiens et al., 2022).

Olivine is a key mineral to deciphering magmatic processes on Earth and Mars as it is the dominant mineral of the mantle of these planets, and it is typically the first phase to crystallize during crustal magmatic processes. Olivine also bears information on magmatic processes including magma differentiation (e.g., Mg# = Mg/[Fe + Mg] atomic ratio, noticed Fo# for forsterite% in olivine) and magma source (e.g., trace elements in olivine). Olivine is common in Martian meteorites (see Udry et al. (2020) and references therein), especially in some shergottites and chassignites, but it has also been observed in nakhlites. Although the presence of olivine is inferred at many localities from orbit (e.g., Ody et al., 2013), it has been relatively scarcely detected by previous in situ missions elsewhere on Mars. The most notable occurrences are the Alpha Particle X-Ray Spectrometer (APXS) detection of olivine in rocks from Gusev crater (McSween et al., 2006, 2008), and some olivine detected in the regolith of dunes at Gale crater (Achilles et al., 2017; Blake et al., 2013; Cousin et al., 2017; Ehlmann et al., 2017; Johnson et al., 2017). At Jezero crater, olivine was first detected in coarse-grained regolith covering the Máaz formation close to the landing site, and later in nearly all rocks from the Séítah formation (Mandon et al., 2022; Wiens et al., 2022). SuperCam and PIXL investigations on two abraded patches from Séítah, called Dourbes and Garde, revealed that this rock is a cumulate that consists primarily of olivine with minor pyroxene (Liu et al., 2022; Wiens et al., 2022). SHERLOC Raman spectroscopy also detected olivine in these patches, exhibiting local yet weak alteration as suggested by the presence of Fe-Mg carbonate texturally associated with olivine in the absence of serpentine (Farley et al., 2022; Scheller et al., 2022). The presence of Fe-Mg carbonate and, overall, the weak alteration of the primary magmatic mineral assemblage has been confirmed and thoroughly investigated by SuperCam observations in the visited areas of Séítah (Clavé et al., 2022; Mandon et al., 2022).

Here, we present and discuss SuperCam data obtained on the olivine-rich Séítah formation. The cumulate nature of Séítah has been locally established by both PIXL (Liu et al., 2022) and SuperCam (Wiens et al., 2022) instruments. PIXL has investigated two abraded patches, while SuperCam has obtained LIBS data on more than 50 rock targets representing more than 500 LIBS points all along the ∼140 m rover path in the Séítah formation, from its contact with the Máaz formation to the more internal parts of the formation. Only a fraction of the SuperCam data was previously presented briefly in the high-level overview of SuperCam activities up to sol 286 by Wiens et al. (2022). We also include analyses from the northwestern (NW) exposures of the Séítah formation, close to the delta front, and long-distance images and VISIR spectroscopy providing additional constraints on the nature of the formation. The LIBS data are complemented by Raman and VISIR spectroscopy analyses to constrain the mineralogy and detect secondary mineral phases due to alteration that have stronger signatures with VISIR spectroscopy (Mandon et al., 2022).

2. SuperCam: A Multi-Technique Instrument for Imaging, Chemistry, and Mineralogy

SuperCam is composed of a Mast Unit (MU), a Body Unit (BU), and a set of calibration targets. The MU includes a laser, a telescope, the remote micro-imager (RMI) and the infrared spectrometer (IRS), whereas the BU includes optics, spectrometers and detectors to analyze the light collected in the UV and visible range. The MU and BU are linked by a 6 m long optical fiber. Details on the MU and BU are given in Maurice et al. (2021) and Wiens et al. (2021) respectively, while calibration targets are described by Manrique et al. (2020) and Cousin et al. (2022). Importantly, all techniques have different analytical footprints, but they are co-boresighted as they use the same telescope for light collection. Only the IR field of view is slightly shifted, as specified below.

In terms of operations, SuperCam analyses are generally run as rasters, which may be lines of 5 or 10 successive points (e.g., 5 × 1, 10 × 1) or a grid of typically 9 points (3 × 3). When combined with Raman and/or VISIR, LIBS is generally performed first, as the laser-induced plasma expansion partially removes dust from the target surface (Lasue et al., 2018; Maurice et al., 2021). Because the LIBS spot is much smaller than the analytical footprint of Raman and VISIR (details given below for each technique), any possible effect of the LIBS laser burst on the target signature for these techniques is negligible (Fau et al., 2019).

2.1. Remote Micro-Imaging (RMI)

Remote Micro-Imaging is described by Wiens et al. (2021) and Maurice et al. (2021). The 110-mm telescope in the MU has a focal length of 563 mm and can take color images of 2,048 × 2,048 pixels with a CMOS camera on a bandwidth from ∼375 to ∼655 nm. The images are divided by a reference flat-field to correct the attenuation factor of ∼5 at the edges (vignetting). The diameter of the circular field-of-view is ∼18.8 mrad. The angular size of the RMI pixels is slightly less than 10 microradians, and the effective image resolution is better than 50 microradians, which represents 0.24 mm at 3 m.

In terms of operations, RMI images are systematically acquired for all analyses with autofocus, and more rarely manual focus, interspersed between the raster points to correct for variations in local topography along a raster. An RMI image is taken on the first point of a raster (before the spectral observations) and one on the last point of the raster (after the spectral observation). Some additional RMI images may be included as needed to cover all points of analyses if the raster is too large to fit on two images.

2.2. LIBS Spectroscopy

SuperCam LIBS is largely inspired by the successful ChemCam LIBS instrument onboard the NASA Curiosity rover (Maurice et al., 2012, 2016; Wiens et al., 2012). SuperCam LIBS uses a pulsed Nd-YAG laser at 1,064 nm with 3–4 ns pulses and a repetition rate generally of 3 Hz but possibly up to 10 Hz. Light emitted by the laser-induced plasma on the target surface is collected by the 110 mm diameter telescope and transferred to the spectrometers in the BU through the optical fiber. The BU is equipped with an optical demultiplexer to separate light based on its wavelength, and with three spectrometers covering complementary spectral ranges: 243.7–345.0 (UV), 379.0–465.0 (VIO), and 532.0–858.8 nm (VIS). The UV and VIO spectrometers have a Czerny-Turner design, whereas the VIS spectrometer is a time-gated transmission spectrometer equipped with an intensified CCD camera. Spectral resolution is around 0.3 nm (Wiens et al., 2021).

For LIBS, a small amount of material is ablated from the target creating plasma. The transient plasma optical emission is at the origin of the LIBS spectrum. In particular, narrow emission lines—characteristic of the ions and atoms present in the plasma—are used to infer the elemental composition of the ablated target. Quantification of elements that are easily excited amongst which are the major rock-forming elements—such as Si, Ti, Al, Fe, Mg, Ca, Na, and K– is possible (Anderson et al., 2022). Furthermore, many other major and minor elements can also be detected, including Mn, H, Cr, Ni, S, Cl, and C (Maurice et al., 2021).

SuperCam's LIBS laser spot size—and therefore the analyzed area—is ∼160 μm in diameter at 2 m and increases to ∼450 μm at 7 m (Maurice et al., 2021). Since more than 75% of LIBS analyses were acquired within 4 m, we assume an average value of ∼250 μm in the following. In general, LIBS observations are performed with 30 laser shots per point, but the spectra collected from the first five shots are discarded to remove dust contamination. As a result, for each point, the mean LIBS spectrum is built by averaging the 25 remaining spectra. Depth of the analytical spot depends mostly on the number of LIBS laser shots as well as on the target optical absorption properties and hardness: it generally reaches tens of μm (Chide et al., 2019, 2020).

Onboard Perseverance, there is a set of 23 standards called SuperCam Calibration Targets dedicated to LIBS, described by Manrique et al. (2020), Cousin et al. (2022), and Madariaga et al. (2022) for the detailed chemical composition. Standards comprise a titanium plate used for wavelength calibration of the spectrometers, for all techniques. They also comprise a set of basaltic glasses doped with various trace elements including Mn and Cr (NTE020106) or Ni (NTE050301) and various minerals, including an apatite, and also rock targets. Of particular interest for this study focused on primary magmatic mineralogy, there are six calibration targets covering primary minerals which can be used as stoichiometric references: PMIOR0507 (orthoclase), PMIAN0106 (andesine), PMIFS0505 (ferrosilite), PMIDN0302 (diopside), PMIEN0602 (enstatite), and PMIFA0306 (olivine). These targets are analyzed routinely with a frequent cadence (e.g., target PMIAN was analyzed 10 times prior to sol 402) to monitor possible evolution of the calibration due to possible thermal and/or mechanical influence on the spectrometers.

2.3. Raman Spectroscopy

For time-resolved Raman and luminescence spectroscopy, the excitation source is the pulsed, frequency-doubled Nd:YAG laser, operating at 532 nm with a 3–4 ns pulse width, 10 mJ pulse energy and 10 Hz pulse repetition rate. The laser is collimated on the target, and not focused as for LIBS, illuminating a surface over a few mm^2. Irradiance at the sample location ranges from 1×10^{10} to 5×10^{10} W m^{-2}, which is below the threshold for laser-induced damage, even for optically absorbing minerals (Fau et al., 2019). The telescope collects light with a field-of-view of 0.75 mrad. Therefore, the analytical footprint diameter (in mm) is equal to 0.75 × distance (in m). Light is then transferred to the optical fiber by an optical system that includes a notch filter. The filter does not remove 100% of the 532 nm laser light; it was not possible to make a filter with perfect 532 nm attenuation while still able to transmit UV and violet light needed for LIBS (Maurice et al., 2021). In the BU, light for Raman and luminescence is directed to a transmission spectrometer via an optical demultiplexer including an edge filter to remove the Rayleigh-scattered laser light (cutoff ≈ 140 cm^{-1}). The transmission spectrometer is a compact design including diffraction gratings, an intensifier, and relay optics that focus light onto a CCD (Wiens et al., 2021). This configuration yields a spectral resolution better than 12 cm^{-1} for the Raman window and allows the collection of luminescence emission signal from 535 to 855 nm. Wavelength calibration is obtained from reference LIBS spectral lines, but an onboard diamond calibration target was specifically designed for Raman to assess the instrument integrity, for example, peak intensity for alignment, peak FWHM for spectral resolution, and peak position for wavelength calibration, as described by Manrique et al. (2020) and Cousin et al. (2022).

SuperCam's Raman spectrometer differs from commercial laboratory instruments in two fundamental ways. First, SuperCam remotely collects Raman signal with a telescope at long distances (i.e., 2–7 m) with large laser spot sizes (i.e., a mm in diameter or greater), while typical commercial laboratory instruments detect Raman signal at short distances (i.e., ∼mm) with small spot sizes (i.e., ∼μm) by using a microscopic approach. Hence, SuperCam Raman generally probes a mixture of mineral phases, depending on grain size, while laboratory instruments generally target a single mineral phase. Second, SuperCam uses a pulsed excitation source combined with a gated detector, while commercial laboratory instruments typically employ continuous-wave excitation sources and detectors. This approach allows for a separation in the time domain since the Raman signal (lifetime $\approx 10^{-15}$ s) is produced during the excitation pulse and other signals like sunlight and luminescence (lifetime $> 10^{-9}$ s) continue after it. Using a short gate (100 ns for SuperCam) that is synchronized with the laser pulse allows efficient elimination of unwanted signals, like superimposing luminescence or sunlight entering the telescope, and optimizes the collection of the Raman signal. Time-resolved spectroscopy further allows the collection of only the luminescence signal by opening the detector gate just after the laser pulse: the Raman signal by then is absent while the luminescence is still present (Beyssac, 2020). Compared with commercial instruments, SuperCam Raman benefits from signal intensification and filtering in the time-domain but uses considerably less excitation, hence receives less signal, because of the non-continuous excitation.

In terms of operations, 100–200 laser shots are recorded as the accumulation on the detector (coadds) of 10 or 20 shots, sometimes duplicated on the same point to have better Signal to Noise Ratio (SNR) for each SuperCam Raman measurement. The CCD exposure time is set to 905 ms to capture the signal from 10 laser pulses in each acquisition, while the intensifier gate is open for 100 ns around each laser pulse, with the gain set at 3,400; these settings were found to result in optimal SNR, while allowing for constraints from operational aspects of the hardware. Unless specified, raw data are presented here without denoising or correction of the instrument response function. Only the non-laser dark spectrum is subtracted from the Raman spectrum and a parasitic signal due to the MU-BU optical fiber is observed. This interfering signal is due to the excitation of the Raman signal of amorphous silica composing the optical fiber by laser light reflected at the target and not filtered out by the notch filter. This interfering signal is composed of several features in the range 100–550 cm^{-1}, at ~800 and ~1,100 cm^{-1}. This parasitic signal is well identified, but removing it automatically is a challenge, as its strength depends on many parameters such as the target reflectivity at 532 nm or the distance to the target.

2.4. VISIR Spectroscopy

SuperCam VISIR is a passive spectroscopy technique based on the analysis of the reflectance of sunlight from the surface of rocks or soils. For this, two spectral regions are analyzed: the visible (VIS) and the Near-Infrared (IR). VIS spectroscopy uses the transmission and blue-violet (VIO) spectrometers to analyze light in the 535–855 and 379–464 nm ranges, respectively. The near-IR range is covered by a specific subsystem located in the MU: the IRS. It uses an acousto-optic tunable filter spectrometer to scan the light in the 1.3–2.6 μm range, with a spectral resolution of 26 cm^{-1}. The technical description of the IRS instrument is given by Fouchet et al. (2022), the calibration aspects including the use of the onboard VISIR calibration targets are detailed by Royer et al. (2023), and an overview of VISIR data obtained on the Jezero crater floor is provided by Mandon et al. (2022).

The light is collected by the Schmidt Cassegrain telescope present in the MU and transmitted by dichroic mirrors to the optical fiber and eventually the BU for the VIS domain, and to the IRS subsystem for the IR domain. The field of view is 0.75 mrad for the transmission spectrometer (VIS), determined by the opical fiber entrance, and 1.15 mrad for the IRS, determined by the pinhole at the entrance of the subsystem. Both field of views are considered as cone angles encircling 65% of the recorded signal from a uniform target. Noticeably, the center of the IRS analytical footprint is shifted by 0.3 mrad compared to the center of the footprint for the other techniques. The footprint diameter is equal to distance (mm) × field of view (mrad) yielding 2.25 and 3.45 mm at 3 m for VIS and IR spectroscopy, respectively (Maurice et al., 2021). Owing to this large analytical footprint, VISIR spectroscopy generally probes a mixture of grains, and not single crystal grains, depending on the grain size of the rock targeted.

In terms of operations, rock targets are selected to ensure correct sunlight illumination at the time of measurement.

3. Assessing Elemental and Mineral Chemistry With LIBS

LIBS spectra from Martian rocks usually contain multiple emission lines from the ionized elements present in the plasma generated by the laser ablation. To go further into the petrological and geochemical interpretation of the LIBS data, the SuperCam team has developed a strategy to retrieve a quantitative evaluation of the elemental composition for the major elements (Anderson et al., 2022). In addition, onboard standards are regularly used to test the detection and quantification strategy. Finally, in cases where the grain size is larger than the LIBS spot size (~220 μm at 3 m), the LIBS-sampled single crystal makes a stoichiometric analysis possible.

3.1. Processing the LIBS Data

An automatic standardized pipeline has been developed to process the LIBS spectra (Anderson et al., 2022). As for Raman, a dark spectrum is first subtracted and an average spectrum minus the five first shots is computed. Spectra from the various spectrometers and spectral windows for the transmission spectrometer are then stitched together, and denoising based on a wavelet transform is applied. Then, a correction of the instrument response function is applied, the continuum is removed and a wavelength calibration is applied. Note that a normalization step is applied by dividing each spectral portion by the total area of the spectrum measured in the corresponding spectral window for the quantification of elemental abundances.

Once these steps have been performed, a series of quality criteria are checked to select LIBS data (also used by Udry et al. (2022)). First, all LIBS spectra exhibiting total emission $<10^{14}$ photons/pulse/mm^2/sr are excluded; these lower values likely indicate poor laser-target coupling and weaker ablation. Points are also excluded if they indicate poor focus in RMI images, or if they show more than 18 motor steps difference between two consecutive focus curves, because this expectedly results in poor focus conditions for the last point acquired before the last auto-focus. Conversion of motor steps into distance depends on the distance to the target as detailed by Maurice et al. (2021). All points analyzed at a distance greater than 6.5 m are also removed from the list to reduce uncertainties related to non-linear physical effects, with laser irradiance varying with the distance.

In addition, in this study, analyses from core tailings and borehole observations were also removed. The laser-target coupling is strongly affected by the surface characteristics of the target, including hardness, absorptivity, and roughness, resulting in non-linear variations in the emission spectra. These physical matrix effects are expected to be especially significant for non-compact, fine-grained materials, such as abrasion and core tailings, in which the shockwave caused by ablation may create significant (mm-size) pits with just a few laser shots.

3.2. Elemental Composition for Major Elements

Quantitative elemental compositions are derived from LIBS spectra using multivariate models involving a library of >1,000 spectra from >320 standards measured using the SuperCam testbed replica in the laboratory. These standards are reference samples with a large variety of known elemental compositions measured using other techniques (Clegg et al., 2017). Using this approach allows us to quantify the major-element oxide compositions (MOC) of Martian targets, that is, the abundances in SiO_2, TiO_2, Al_2O_3, FeOT, MgO, CaO, Na_2O, and K_2O. FeOT refers here to total iron quantified as monoxide regardless of its actual oxidation state, which is not determined by LIBS. Unless specified, the elemental abundances in the following are used without normalization. Sums of the eight major-element oxides that fall significantly below 100 wt% may be suggestive of the presence of other constituents such as CO_2, SO_3, Cl, H_2O/OH, P_2O_5, MnO, and other minor or trace elements. In the following, unless specified, we removed data with MOC totals lower than 80 wt% that may be due to missing chemical species (e.g., OH, SO_4^{2-}, CO_3^{2-}), likely associated with accessory or secondary phases. The detailed description of the MOC approach is given by Anderson et al. (2022) and a first application to the Jezero Crater floor data was discussed by Wiens et al. (2022).

Targets, defined here as rasters that may or may not be from distinct rocks, have been grouped by geographic proximity and/or distance to the southern contact between the Máaz and Séítah formations along the Artuby ridge as listed in Table S1: Entrevaux (3 targets) just below Artuby ridge then Issole (29 targets), Bastide (8 targets), and Brac (18 targets) with increasing distance to Artuby, as shown in Figure 1. There are also a few isolated targets in between these groups. The last group is NW Séítah (3 targets) that was visited on sols 417–420. LIBS analyses for Séítah are summarized in Table S2.

The data processing pipeline also returns MOC abundances for individual spectra associated with each laser shot in the burst of 30 performed on each point of the raster: this is referred to as the shot-to-shot MOC. Because MOC-derived abundances were developed on averaged spectra, which are overall better in SNR than the shot-to-shot spectra, this shot-to-shot MOC compositions must be considered with caution. During the analysis, the LIBS laser may ablate significantly into the target, up to hundreds of μm depending on the target properties (Chide et al., 2019, 2020). Shot-to-shot MOC constitutes an interesting data set to investigate depth profile compositions. This may help to validate whether the LIBS laser sampled a single crystal grain or mineral mixtures, by looking at the variability of some elements (e.g., Si, Fe, and Mg for olivine) during the laser burst.

3.3. Uncertainties of the Derived Element Quantification

Uncertainties of the derived MOC elemental abundances are quantified by the accuracy and precision. The accuracy may be measured by the root mean squared error of the prediction of the suite of standards that were not used to train the multivariate model, as presented by Anderson et al. (2022). Accuracy is useful when one compares MOC elemental abundances with stoichiometric mineral compositions or with abundances derived from other instruments, for a given target. On Mars, accuracy is tested using regular analysis of the onboard calibration targets. General averaged one-sigma accuracies for SiO_2, TiO_2, Al_2O_3, FeOT, MgO, CaO, Na_2O, and K_2O are ±6.1, 0.3, 1.8, 3.1, 1.1, 1.3, 0.5, and 0.6 wt%, respectively (Anderson et al., 2022). Precision may be defined as the distribution of individual results around the average value. Here, precisions were obtained from standard deviations of elemental abundances derived from analyses made on a large number of standards in the laboratory and on rover calibration targets (Anderson et al., 2022). General precision for SiO_2, TiO_2, Al_2O_3, FeOT, MgO, CaO, Na_2O, and K_2O are ±1.6, 0.06, 0.7, 1.3, 0.5, 0.5, 0.3, 0.3 wt%, respectively (using the largest values from Anderson et al., 2022). These precisions were propagated from oxide wt% to molar abundances where applicable.

In general, SuperCam LIBS elemental abundances using the current calibration model are substantially more precise than they are accurate. This allows for a confident comparison of Martian data with each other and with the calibration targets, especially for data in the 2–6.5 m range, where most data have been acquired.

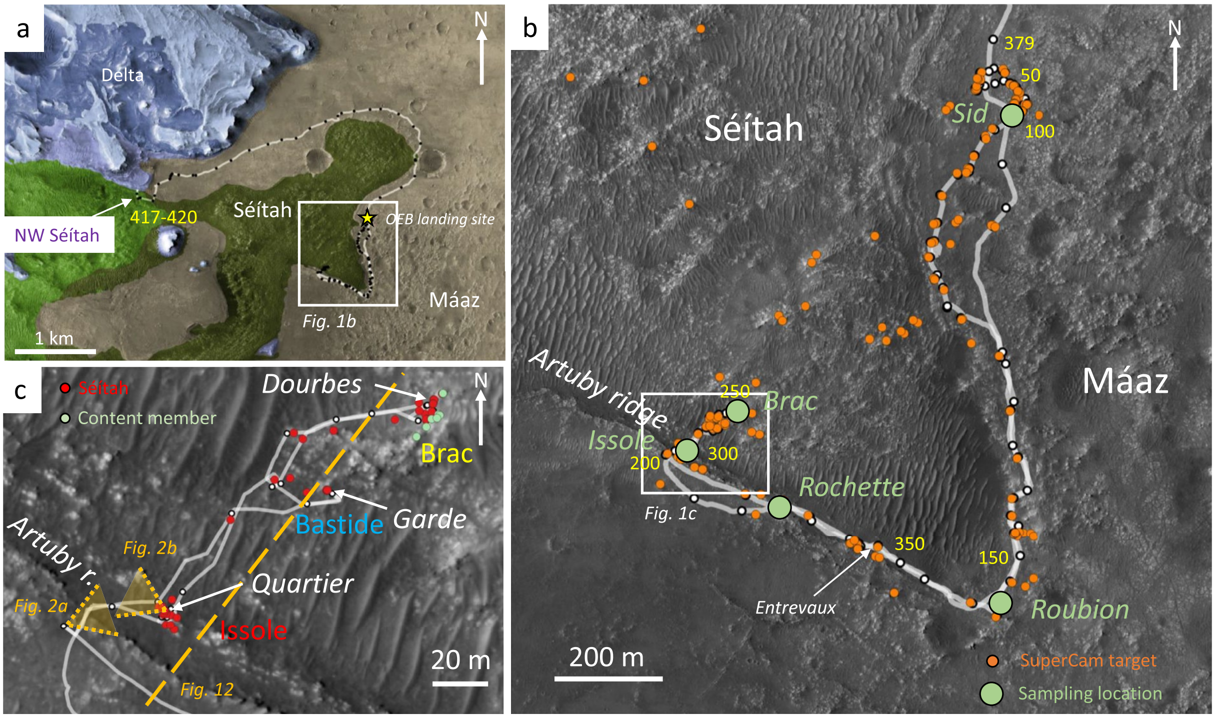

Figure 1. Maps of Jezero crater and areas investigated by Perseverance on the crater floor. (a) Geological map of the crater floor showing the delta (blue), Máaz (brown), and Séítah (green) formations. The Octavia E. Butler (OEB) landing site, the rover traverse and stops (dots) are indicated. The northwestern Séítah visited on sols 417–420 is indicated. (b) Enlarged area of the rover traverse overlain on a HiRISE mosaic. Rover stops (white circles) with sol numbers (every 50, yellow), all SuperCam targets including long-distance ones (orange circles), and outcrops for samples collection (green) are indicated. (c) Enlarged area of the Séítah region visited by the rover on a HiRISE mosaic. SuperCam targets used in this study are indicated for Séítah (red circles) and the Content member, which is an equivalent of the Máaz formation (green), is indicated along the rover traverse with rover stops indicated (white circles). The three main outcrops visited (Issole, Bastide, and Brac) and corresponding abraded patches (Quartier, Garde, and Dourbes) are located. The color code (red = Issole, blue = Bastide, and yellow = Brac) is the same used for all figures. Approximate field of view of the MastCam-Z images depicted in Figure 2 are indicated in orange, as well as the trace of the cross-section presented in Figure 12 (orange dashed line).

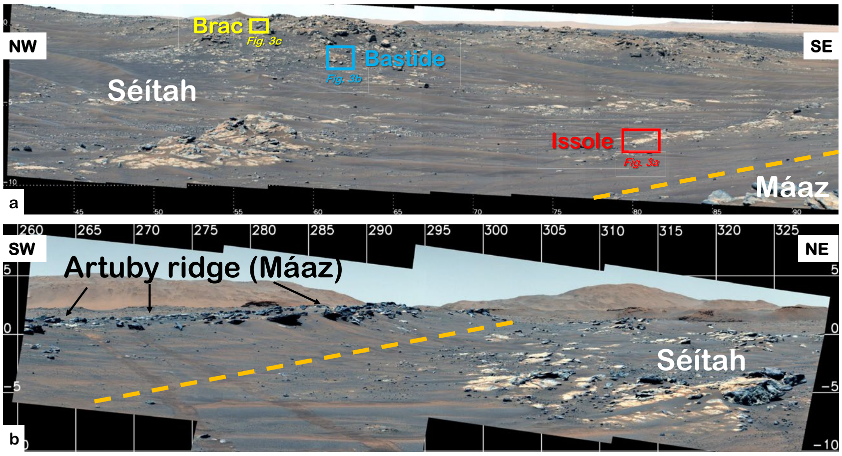

Figure 2. MastCam-Z mosaics of the boundary between the Máaz and Séítah formations at Artuby ridge. Rover position and approximate field of view are indicated on Figure 1c. (a) View from Artuby ridge toward the NE showing the Séítah formation and the three main outcrops visited (Issole, Bastide, and Brac). (b) View from Séítah toward Artuby ridge toward the northwestern. In both images, the approximate position of the contact between Máaz and Séítah is located with an orange dashed line as the contact is covered by sand ripples. See Figure 1 for location.

3.4. Stoichiometric Analysis

When the grain size of the targeted rock is sufficiently large, that is, larger than the LIBS spot size (>220 μm at 3 m), the laser may sample a single crystal grain, enabling a stoichiometric analysis of this crystal from the MOC derived abundances. All MOC data are screened in ternary diagrams as well as based on some appropriate elemental molar ratios in order to detect MOC compositions consistent with pure crystals, also used in Udry et al. (2022). After this screening, a series of criteria depending on the possible stoichiometry (see Table S3) is applied to the analysis to make sure the data are consistent with a single crystal phase. In addition, the RMI is carefully analyzed to check whether a crystal grain can be recognized directly on the image at the position of the LIBS analysis. In addition, the shot-to-shot MOC data are monitored to check that the MOC composition is not resulting from a mineral mixture but that relevant elements (e.g., Fe, Mg, Si for olivine) are constant throughout the laser burst. If all criteria are met, then a stoichiometry is calculated for the point considered assuming 4 oxygens for olivine and 6 for pyroxene, and that all Fe is in the form FeII. Although some points may be close to a plagioclase composition, we did not detect any point with an elemental composition consistent with pure plagioclase.

3.5. Detecting Minor and Trace Elements With LIBS

Many trace or minor elements contribute emission lines to the plasma and may be detected by LIBS with various limits of detection (Cremers & Radziemski, 2013; Payré et al., 2017). No quantification is available yet for the SuperCam instrument. For instance, C lines may be used to investigate carbonates (Clavé et al., 2022) and S and Cl lines are present and may be due to the presence of sulfates or sulfides, and perchlorates detected by other instruments (Tice et al., 2022).

Here, we use the detection of H to which LIBS is highly sensitive, as demonstrated for ChemCam at Gale crater (e.g., Rapin et al., 2017). For this, we compute the area of the H line at 656.5 nm using a Levenberg-Marquard scheme. Likewise, the detection of Mn and Cr is based on the total area of the Mn triplet around 403.5 nm and the area of the Cr line at 425.55 nm, respectively. Mn is notably incorporated in pyroxene and olivine, while high amounts of Cr might indicate the presence of Cr-rich minerals, such as chromite or some spinels.

4. Geological Background

4.1. The Nili Fossae Region and the Regional Olivine-Carbonate Unit

Jezero crater is located in the Noachian Nili Fossae region of Mars, which is close to the Isidis Planitia impact basin. Nili Fossae hosts the largest exposure of olivine on Mars detected from orbit, which is locally associated with the detection of pyroxene and secondary phases such as carbonate and clay. A brief review is given here with a focus on primary mineralogy, but more information from orbital data may be found in the recent articles by Brown et al. (2020), Mandon et al. (2020), Horgan et al. (2020) or Tarnas et al. (2021), and references therein.

Olivine has been detected by orbital thermal and near infrared spectroscopy (Hoefen et al., 2003; Mustard et al., 2005). The estimated olivine abundance varies depending on the technique: unmixing models from Thermal Emission Spectrometers yield 10% olivine (Salvatore et al., 2018) to 30% (Hoefen et al., 2003), while radiative transfer modeling of the OMEGA near infared spectra yields estimates of 40% (Poulet et al., 2009) with mm-sized grains, and data from the CRISM instrument provide an estimated abundance of 20%–25% olivine (Edwards & Ehlmann, 2015). These studies assume that olivine is a dominant phase in these rocks and that the grain-size is generally sand-sized, in the range of ∼0.5 mm to a few mm.

Estimating the Fo# of olivine from VISIR reflectance orbital spectra remains a challenging exercise. At the same time, Fo# is an important parameter that may shift the position of the characteristic 1 μm absorption band in reflectance spectra of olivine, but this position is also a function of grain size and/or the presence of other minerals complicating the spectra. In general, most studies have suggested that olivine in the region of Jezero crater is Mg-rich, but the uncertainty on Fo# remains high. In a recent study, Brown et al. (2020) reviewed the available observations and reinvestigated orbital data in light of experimental constraints, and suggested that olivine in the region of Jezero crater likely has grain sizes of 0.5–1 mm with olivine Fo# in the range 40–66.

The other main primary magmatic phase detected from orbit in the olivine-carbonate unit is pyroxene, which was initially detected by Mustard et al. (2005) for Mars in general, and more specifically by Mustard et al. (2009) in the Isidis region. Both low-Ca (orthopyroxene, pigeonite) and high-Ca (clinopyroxene) pyroxenes are detected, often mixed with olivine, but assessing their respective proportions from these data remains a challenging task. Furthermore, feldspar minerals are featureless phases for orbital VISIR spectroscopy, although we know that they are present on Mars based on in situ exploration (Sautter et al., 2015), and from the presence of maskelynite and feldspar in Martian meteorites (see Udry et al. (2020) and references therein). Finally, secondary phases resulting from alteration are detected in this formation, among which carbonate and clay phases are dominant. Regardless of these secondary phases, olivine signatures from orbit remain remarkably pristine, suggesting that alteration was minimal, at least locally.

Various scenarios have been proposed for the emplacement of the regional olivine-carbonate unit, ranging from igneous to sedimentary. These scenarios include large-scale volcanic flows (Hamilton & Christensen, 2005), Isidis basin impact melt (Mustard et al., 2007, 2009), and clastic (Rogers et al., 2018) to ashfall or pyroclastic deposits (Kremer et al., 2019; Mandon et al., 2020). On the Jezero crater floor specifically, preferred hypotheses for the origin of the Séítah formation prior to landing of the Perseverance rover included volcanic ash deposition, aeolian deposition, or deposition by fluvio-lacustrine processes (Stack et al., 2020).

4.2. Geology of Jezero Crater Floor

Perseverance landed in the southeastern quarter of the landing ellipse close to the boundary between the two main formations of the Jezero crater floor: the Crater floor—Fracture rough (Cf-Fr) and Crater floor—Fractured 1 formations following the terminology of Stack et al. (2020). These units refer to the dark-toned crater floor and light toned units of Goudge et al. (2015), and are now respectively named Máaz and Séítah formations by the Perseverance team (Farley et al., 2022; Sun et al., 2023). From orbit, these units have distinct geomorphic and mineralogic signatures. Máaz occupies the vast majority of the Jezero crater floor, and is locally covered by undifferentiated regolith and sand ripples. Hyperspectral data from orbit suggest that the mineralogy of Máaz is dominated by high-Ca pyroxene with minor low-Ca pyroxene (Goudge et al., 2015; Horgan et al., 2020; Mandon et al., 2020). The contact between Máaz formation and the underlying Séítah formation is remarkably sharp in HiRISE images, which also highlights the differences in geomorphic expression of the two formations: whereas the Máaz formation is broadly planar and retains clear evidence of cratering, Séítah retains an irregular topographic expression and lacks clear evidence of crater retention. Similarly, whereas the Máaz formation shows distinct evidence of layering—visible from orbit, especially at the interface between the two formations—the Séítah formation is primarily massive, with no clear stratification visible from orbit. The mineral signature of the Séítah formation from orbit is also dominated by olivine, both within bedrock exposure and local sand dunes, suggesting that the olivine content in the bedrock is significant and/or that olivine grains are large.

The first months of exploration have largely confirmed the mineralogical observations from orbit, showing that Máaz and Séítah are weakly to moderately altered igneous formations (Farley et al., 2022; Scheller et al., 2022; Wiens et al., 2022). The Máaz formation appears to be composed of lava flows with basaltic to basaltic-andesite chemistry in which the main minerals detected are pyroxene and plagioclase (Udry et al., 2022). By contrast, the Séítah formation appears to be composed of cumulate rocks dominated by olivine and some pyroxene (Liu et al., 2022; this study). At the time of writing, the structural relationship between these two formations and the Jezero delta is not yet established, but the current hypotheses suggest that they were emplaced before the formation of the delta (Farley et al., 2022; Holm-Alwmark et al., 2021; Quantin-Nataf et al., 2023).

4.3. The Séítah Formation

Perseverance landed close to one of the two main exposures of the Séítah formation that lies close to the delta (Figure 1). The Octavia E. Butler landing site is actually located just a few tens of meters east of the Máaz-Séítah contact. However, this transition consists of a small, yet sharp, escarpment and a depression full of sand ripples that prevented a direct traverse into the Séítah formation close to the landing site. A region south of the landing site, called Artuby Ridge, was identified as the most promising site to explore both the stratigraphy of the Máaz formation and its relationship with the underlying Séítah formation (Sun et al., 2023). During the southward traverse, several long-distance images of Séitah by MastCam-Z and RMI were acquired, some with VISIR spectroscopy, which provided a first glance into the structure and mineralogy of the core of this formation and other inaccessible areas. An overview of the structure and stratigraphy is given here.

Along Artuby ridge, the Séítah formation underlies strata of the Máaz formation dipping toward the southwest (Figure 2). Within the internal regions of the area mapped as Séítah formation, however, exposures of Séítah bedrock occur topographically higher than the surrounding Máaz formation. Perseverance first encountered a rock from Séítah on sol 173 with the Entrevaux target, then again on sol 178 with target Aiguines, before entering the formation on sol 202. Criteria to determine whether a rock along the Máaz/Séítah boundary belongs to Séítah are (a) high Mg content of the rock, (b) evidence for olivine based on LIBS and/or VISIR, and (c) a granular texture of the rock. These two rocks (Entrevaux and Aiguines), first noted for their distinct composition as compared to rocks of the Máaz formation, are located in a broad depression below the Artuby ridge. They might represent the rocks from Séítah closest to the Máaz formation. Perseverance then started a traverse into Séítah on sol 202, which lasted until sol 340, including a period of solar conjunction during which rover activities were suspended.

The scientific survey of the Séítah formation consists of a ∼140 m long trip heading NE from the point of entrance along Artuby ridge. SuperCam activities were mostly focused on three areas at the Issole, Bastide, and Brac outcrops (Figure 1), within working spaces corresponding to the Quartier, Garde, and Dourbes abraded patches, respectively (Figure 2). On sols 417–420, when headed toward the delta, the rover again traversed the Séítah formation with a group of 3 targets called NW Séítah (Figure 1). In the following section, LIBS observations are grouped and discussed for these main workspaces; a few targets which were analyzed in between these main regions are also discussed.

Strata of the NW-SE-trending Artuby ridge are defined as the lowermost strata of the Máaz formation (Alwmark et al., 2023; Horgan et al., 2023; Udry et al., 2022). The stratigraphic contact between Séítah and Máaz is located along an escarpment that is covered by regolith and sand ripples, which precludes direct observation of the contact (Figure 2). The Séítah targets analyzed by SuperCam closest to the contact with Máaz are Entrevaux (sol 173), Aiguines (sol 178), and Chaudon (sol 343). These rocks are located within 10 m of the contact, although only Aiguines appears to be in place and not a float rock. The Issole region is a bit further from the contact and includes targets in the range of 10–22 m from the contact. Issole was visited first on sol 202 and then on sol 287 to sol 340. Two paired samples were collected at Issole, Robine, and Malay cores (Simon et al., 2023), both from the vicinity of the Quartier abraded patch. The Issole outcrop is a few meters wide and consists of relatively dusty flat rocks with bedding dipping about 10° toward the SW (Figure 3a). Several targets within the region, including the Quartier abraded patch, were analyzed to document outcrop diversity. The rover then moved toward the second workspace, called Bastide, with targets located between 80 and 90 m from the contact with Artuby, including the Garde abraded patch. This outcrop consists of stratified rocks with bedding gently dipping about 5–10° toward the SW (Figure 3b). The rocks are relatively dusty on their top horizontal surface but appear dust-free on vertical faces. Stratification is more evident than at Issole; layers are a few centimeters thick and are identified by primary parallel fractures within the outcrop and appear consistent throughout the outcrop.

The rover then continued to climb a gentle slope toward the Brac workspace, which is the furthest from the Artuby ridge with targets ranging between 130 and 140 m from Artuby. The Brac workspace is in the innermost part of Séítah explored by Perseverance. The Brac workspace is distinctly more massive. The rocks are still layered, but the thicknesses of the layers are greater than those observed at Issole and Bastide (Figure 3c). Many targets were analyzed in this outcrop, especially on the rock called Brac, which hosts the Dourbes abraded patch, and where the two cores, Salette and Coulettes, were collected. Massive rocks of the Brac outcrop region are located below a distinct stratigraphic member called Content. This member is composed of massive pitted rocks with chemistry and VISIR signature much more similar to Máaz than to Séítah. The Content member is essentially an equivalent to the Máaz formation and is discussed in detail by Udry et al. (2022). Noticeably, the contact is apparently due to the pitted aspect of the Content member, but it does not show any other evident structural feature to characterize it. Finally, NW Séítah outcrops consist mostly of dispersed, locally massive rocks outcropping among sand ripples (Figure 3d).

5. Results

5.1. Structure and Mineralogy of Inner Séítah From Long-Distance Observations

Here, we present the SuperCam long-distance analyses for the parts of the Séítah core formation that were not visited by the rover and thus largely inaccessible for other instruments, apart from MastCam-Z (J. F. Bell et al., 2022). Figure 4 presents long-distance RMI and VISIR observations in remote localities of Séítah. These long-distance observations were obtained when the rover was driving on the Máaz formation from the landing

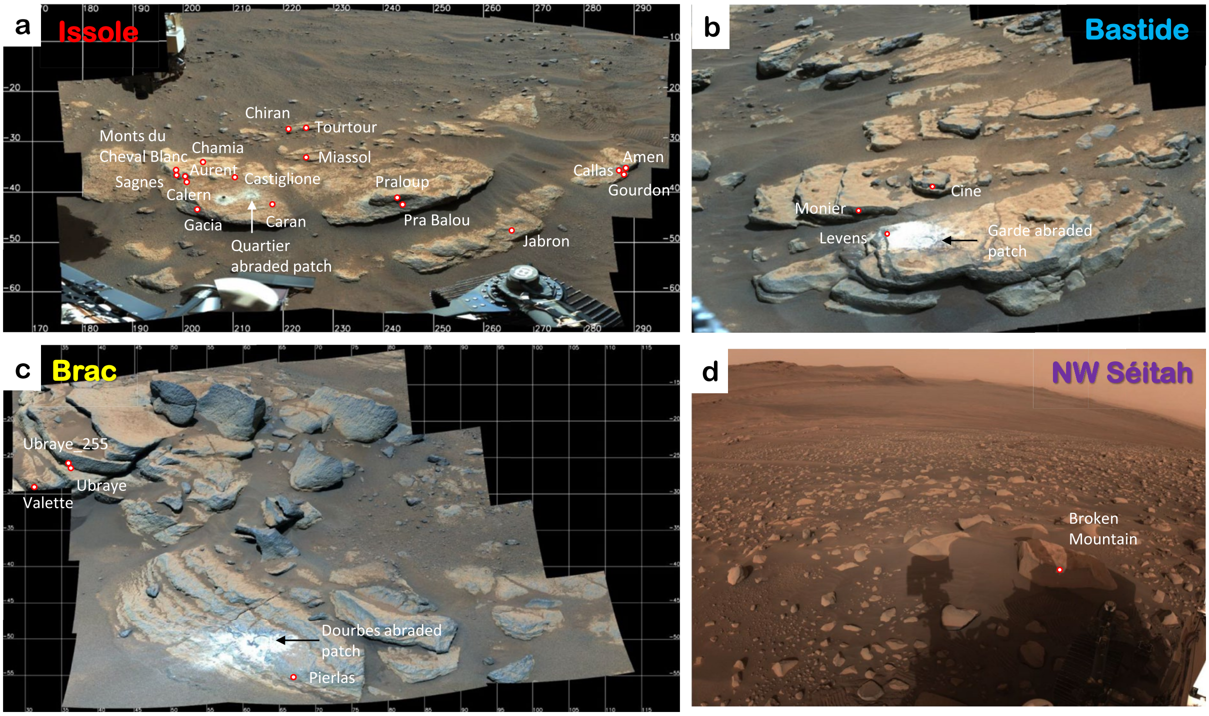

Figure 3. MastCam-Z mosaics of the (a) Issole, (b) Bastide, and (c) Brac outcrops. NavCam image of northwestern (d) Séítah near the Broken Mountain target (sol 420). On each image, SuperCam targets are indicated. For scale, the drill holes and abrasion patches are ∼23 and 50 mm in diameter, respectively.

site toward the entrance to Séítah along Artuby ridge. Locally, RMI images show large exposures of dusty pavers locally exhibiting horizontal layering, such as in the sol 120 RMI (Figure 4b). More generally, these RMI images show that the Séítah formation rocks are broadly stratified, as observed in the image mosaics taken on sols 69 (Figure 4c) and 96 (Figure 4d), which shows relatively fine layering with apparently horizontal layers measuring a few tens of centimeters in thickness. Thinner layers may be present but are unable to be resolved on these images. The sol 69 RMI shows that thicker strata occur above the thin layers and form the crest of the topographic ridge. Such thicker layers at the top of ridges, and above thinner layers, were observed in other RMI images, and may represent a common theme in exposures of the Séítah formation. In other RMI images, Séítah appears as relatively chaotic with no particular structure with blocks of rocks outcropping among the regolith dunes. Noticeably, in nearly all RMI images, the visible strata appear subhorizontal, which suggests that in the inner part imaged, Séítah is a flat-lying formation.

Figure 4e presents some representative long-distance VISIR spectra. These spectra were carefully selected based on the RMI images to have the analytical footprint of VISIR including only rock, and no regolith or other loose material. All these spectra display a broad absorption band centered at ∼1 μm indicative of olivine. In addition, above 1.8 μm, the spectra are generally not flat and exhibit a decreasing slope together with a strong 1.9 μm absorption feature due to hydration. Some weaker features may be observed in some spectra; they mostly correspond to metal-OH absorption features (see Mandon et al. (2022), for further discussion).

5.2. Textural Analysis of Rocks

Here, we provide textural analysis of Séítah rocks based on RMI images of natural surfaces, with additional information from the WATSON camera and RMI images of abrasion patches. Targets Cine (sol 206) and Penne (sol 211), both of which correspond to vertical surfaces with only minor modifications by wind abrasion, provide the greatest textural details (Figure 5).

Séítah rocks are layered along the rover traverse. Layering may be thin, typically a few cm, while the thickest layers locally reach a few tens of cm, typically 40–50 cm. Noticeably, while layering seems relatively thin and constant from Issole to Bastide, its thickness increases going toward Brac in the topographically higher, yet

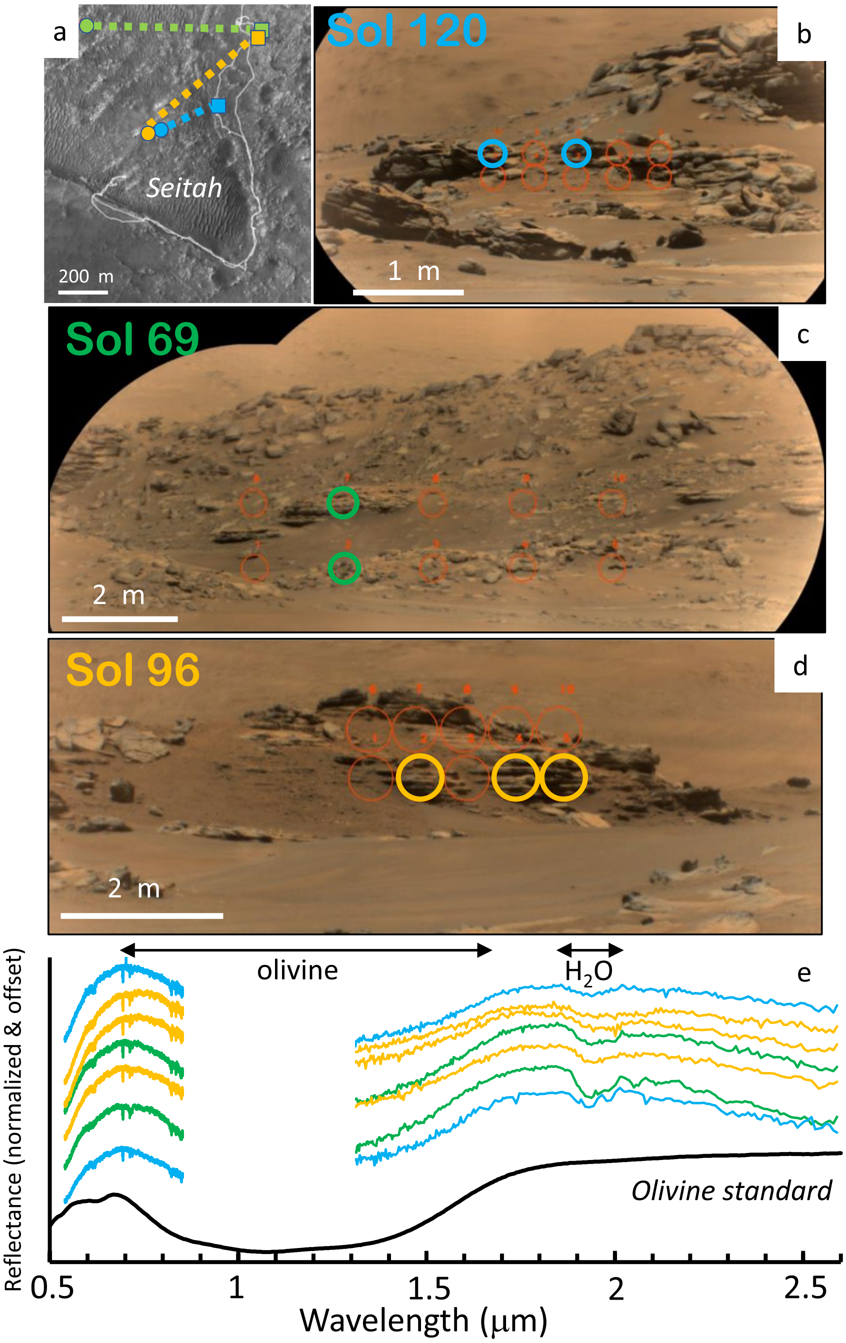

Figure 4. SuperCam long-distance remote micro-imager-Supercam Visible and Infrared reflectance (RMI-VISIR). (a) Localization of long-distance RMI-VISIR performed on (b) sol 120, (c) sol 69, and (d) sol 96 and corresponding rover positions. On each RMI image, the IR analytical footprint for all points of the raster is indicated as red circles with point number. The points sampling rocks and not regolith/sand are underlined in color, and the corresponding VISIR spectra (normalized and offset) are depicted in panel (d) with a spectrum of an olivine standard (RELAB C1PO47). All these long-distance VISIR spectra exhibit a strong absorption band at ∼1 μm indicative of olivine similar to the reference spectrum as well as a hydration band at ∼1.9 μm.

stratigraphically older part of the Séítah formation. Natural and abraded surfaces show discrete angular to subangular grains. Grains show planar, smooth surfaces and distinctly sharp edges on natural surfaces (Figure 5). These planar surfaces record no distinct orientation on the rock surface, indicating that they result from the nature of the grains, rather than the surficial weathering of the outcrop. Altogether, these observations suggest that individual grains are predominantly monocrystalline, and that the grain shape records natural faceted crystal morphologies.

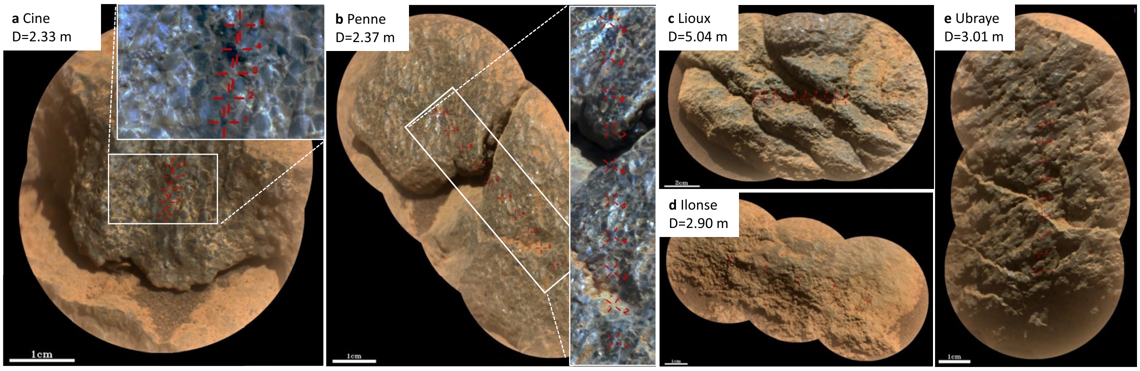

Figure 5. Images by SuperCam Remote Micro-Imager of various rock targets in Séítah in natural colors. The close-up in panels (a, b) have colors modified by Gaussian color-stretching. (a) Cine, sol 206; (b) Penne, sol 211; (c) Lioux, sol 204; (d) Ilonse, sol 256; and (e) Ubraye, sol 253. For each target, distance (in m) is specified.

Figure 5 depicts some representative RMI images and texture for Séítah rocks. Within the rock, individual crystals are not clearly interlocking at the RMI scale of detection, but rather form a closely packed accumulation where planar grain edges abut adjacent grains. More rarely, grains oriented at angles to each other can be found. Intercrystalline material in these regions contains either an accumulation of smaller grains or (more typically) a smooth red-to-brown matrix that is typically observed between the grains (Figure 5). The generally smooth, yet distinctly non-planar, weathering of this matrix material suggests a very fine grained or potentially waxy material. Individual crystals within the rock are typically dark gray to translucent yellow-gray in color (blue in color stretched images) that mostly correspond to olivine (see below), with a subordinate percentage of grains showing a distinctly browner tone on natural surfaces. Subordinate brown grains are also typically less angular than the dark gray grains. These colors are apparent and may be partly influenced by dust.

Grain size analysis has been performed for 17 distinct targets within the Séítah formation: 100 to 600 grains, with an average of 330 grains counted on each target (Table S4). All samples recorded generally equant grains. Equant grains are determined by the length of the long (L) axis with respect to the intermediate (I) axis (the longest axis measurable perpendicular to the long axis), where $I/L > 0.67$ is defined as equant. For all samples, $I/L > 0.77$, with standard deviation is typically <0.1. In total, the average grain size of Séítah rocks is 1.26 ± 0.25 mm. Examination of grain sizes within the context of geographic location and stratigraphic position, however, shows distinct patterns in grain size. Grain size of the stratigraphically lowest materials (i.e., materials that were stratigraphically lower than the position of the rover at Bastide) are distinctly finer (Bastide L in Table S4, 1.19 ± 0.83–1.36 ± 0.27 mm) than those directly at the Bastide location (Bastide in Table S4, 1.60 ± 0.22–1.66 ± 0.27 mm). Samples from the stratigraphically deepest locality in the Brac region are in the range 1.22 ± 0.21–1.45 ± 0.26 mm. Samples from the stratigraphically highest Issole locality are finer in the range 0.75 ± 0.15–0.95 ± 0.20 mm. Two samples within the Brac and Issole regions, respectively Ubraye sol 253 and Bezaudun sol 286, appear to be exceptions to this trend, with grain sizes more similar to those at Bastide (1.58 ± 0.31 and 1.50 ± 0.22 mm, respectively). Note that Bezaudun, however, is a distinctly displaced float block, and may very well represent Bastide locality material.

5.3. Chemistry

Table 1 presents the average composition of the main groups of targets from LIBS analyses. Figure 6 presents the chemical data obtained from LIBS and the average value for the main groups of targets as defined above. In the Total alkali-silica (TAS), $Na_2O + K_2O$ versus SiO_2 diagram (Figure 6a), nearly all targets have $Na_2O + K_2O$ totals that cluster in the range 0.5–3 wt.%. Targets from Issole, NW Séítah and Entrevaux (below Artuby) groups have generally slightly higher $Na_2O + K_2O$ compared to Bastide and Brac. For SiO_2, most targets are clustered in the range 40–50 wt.%, with highest content for Bastide and Brac. Altogether, these targets fall in the picro-basalt to basalt field of this diagram, but this nomenclature is defined for volcanic rocks and does not apply if these rocks are cumulates. The bulk composition of these rocks is actually rather mafic to ultra-mafic as shown below.

The rocks from Séítah are generally Mg-rich with some variations along the transect (Figure 6 and Table 1). For each group, we present here a mean value for abundance with a standard deviation from the mean. Issole has the

Table 1
Laser-Induced Breakdown Spectroscopy Chemical Compositions of the Groups in the Séítah Formation

	Entrevaux		Issole		Bastide		Brac		NW seitah	
	Mean	*Stdev*	Mean	*Stdev*	Mean	*Stdev*	Mean	*Stdev*	Mean	*Stdev*
nb targets	3		29		9		18		3	
SiO_2	47.54	*2.22*	44.31	*3.66*	46.00	*2.75*	46.18	*2.00*	45.20	*2.05*
TiO_2	0.33	*0.14*	0.24	*0.17*	0.18	*0.09*	0.15	*0.11*	0.13	*0.10*
Al_2O_3	5.60	*1.46*	5.09	*1.96*	3.71	*0.95*	3.57	*1.33*	4.05	*1.29*
FeOT	21.24	*3.77*	23.58	*4.78*	23.07	*3.09*	23.55	*4.21*	21.57	*1.98*
MgO	18.80	*5.83*	15.11	*6.34*	20.10	*5.59*	23.75	*4.04*	22.94	*12.06*
CaO	5.27	*2.58*	3.76	*1.59*	4.07	*2.47*	3.59	*2.24*	3.91	*2.06*
Na_2O	1.95	*0.43*	1.80	*0.56*	1.12	*0.43*	1.21	*0.44*	1.14	*0.42*
K_2O	0.43	*0.25*	0.56	*0.25*	0.29	*0.38*	0.44	*0.36*	0.29	*0.28*
Al/Si	0.14	*0.04*	0.14	*0.06*	0.10	*0.03*	0.09	*0.03*	0.11	*0.04*
(Fe + Mg)/Si	0.96	*0.24*	0.97	*0.31*	1.07	*0.19*	1.20	*0.19*	1.18	*0.43*
Mg#	61	*5*	52	*8*	60	*5*	64	*4*	62	*14*

Note. See Table S1 for the list of targets composing each group. See text for details on precision and accuracy of chemical quantification from LIBS data.

lowest average MgO at 15.1 ± 6.3 wt% with substantial variability from 6 wt% (target Chamia sol 327) up to 28 wt% (target Chabran sol 335). Bastide has an intermediate MgO with an average of 20.1 ± 5.6 wt% with significant variability from 12.6 wt% (target Levens sol 205) up to 29 wt% (target Lioux sol 204). Brac has the highest average MgO at 23.8 ± 4 wt%, somewhat variable in the range 17.0 wt% (target Dourbes sol 259) up to 31.5 wt% (target Chasteuil sol 274). Targets from Entrevaux and NW Séítah groups show substantial variability despite the lower number of targets and have intermediate average MgO contents at 18.8 ± 5.8 and 22.9 ± 12.1 wt%, respectively. In all these groups, FeOT is relatively high. Remarkably, FeOT is nearly constant among the groups with an average content ranging from 21.2 ± 3.8 wt% for the Entrevaux group to 23.6 ± 4.8 wt% for the Issole group. There might be a subtle positive correlation between FeOT and MgO. Despite similarities in the average FeOT, there is significant variability in FeOT among targets within the same group, especially in the Issole group, with the lowest content of 14 wt% for Jabron sol 309 and the highest content of 34.7 wt% for PraBalou sol 323.

Séítah rocks are also moderately rich in CaO and the various groups have average CaO content of 3.6 ± 2.2 wt% for Brac, 4.1 ± 2.5 wt% for Bastide, and a higher average CaO content for the Entrevaux group at 5.3 ± 2.6 wt%. Again, variability is observed within each group, and even in the same abraded patch with CaO below 1 wt% for Dourbes sol 268 to CaO higher than 8 wt% for Dourbes sol 259. Finally, Séítah rocks are moderately rich in Al_2O_3, and there is variability among the groups: the highest average contents are observed in Issole and Entrevaux at 5.1 ± 2 and 5.6 ± 1.5 wt%, respectively, while the lowest contents are observed in Bastide and Brac at 3.7 ± 1 and 3.6 ± 1.3 wt% Al_2O_3, respectively. Again, some variability is observed, especially in the Issole group with endmember values from 1.3 (PraBalou) to 10 wt% for Jabron. Note that for each group, most targets are from adjacent rocks, and sometimes include an abraded patch (Figure 3). The variability observed among these relatively closely spaced targets may reflect intrinsic chemical heterogeneity at the scale of the LIBS spot, or grain size larger than LIBS spot size and variability among the crystals analyzed (see next section).

Figure 7 depicts the Al/Si versus (Fe + Mg)/Si molar ratio for each analysis point as well as for the calibration targets on Mars and using other techniques in the laboratory (here we use the Laser Ablation Inductively coupled Plasma Mass Spectrometer [LA-ICP-MS] data from Cousin et al. (2022) as the reference). In such a diagram, mafic minerals such as olivine or pyroxene plot along the *x*-axis, while felsic minerals such as feldspars plot along the *y*-axis. This diagram offers the opportunity to test the precision and accuracy of the LIBS MOC calibration. The andesine standard (PMIAN) on Mars has a higher Al/Si in the 0.62–0.72 range compared with the laboratory value of 0.46, and slightly higher (Fe + Mg)/Si in the range 0.04–0.12 compared with 0.02 in the laboratory. The diopside standard

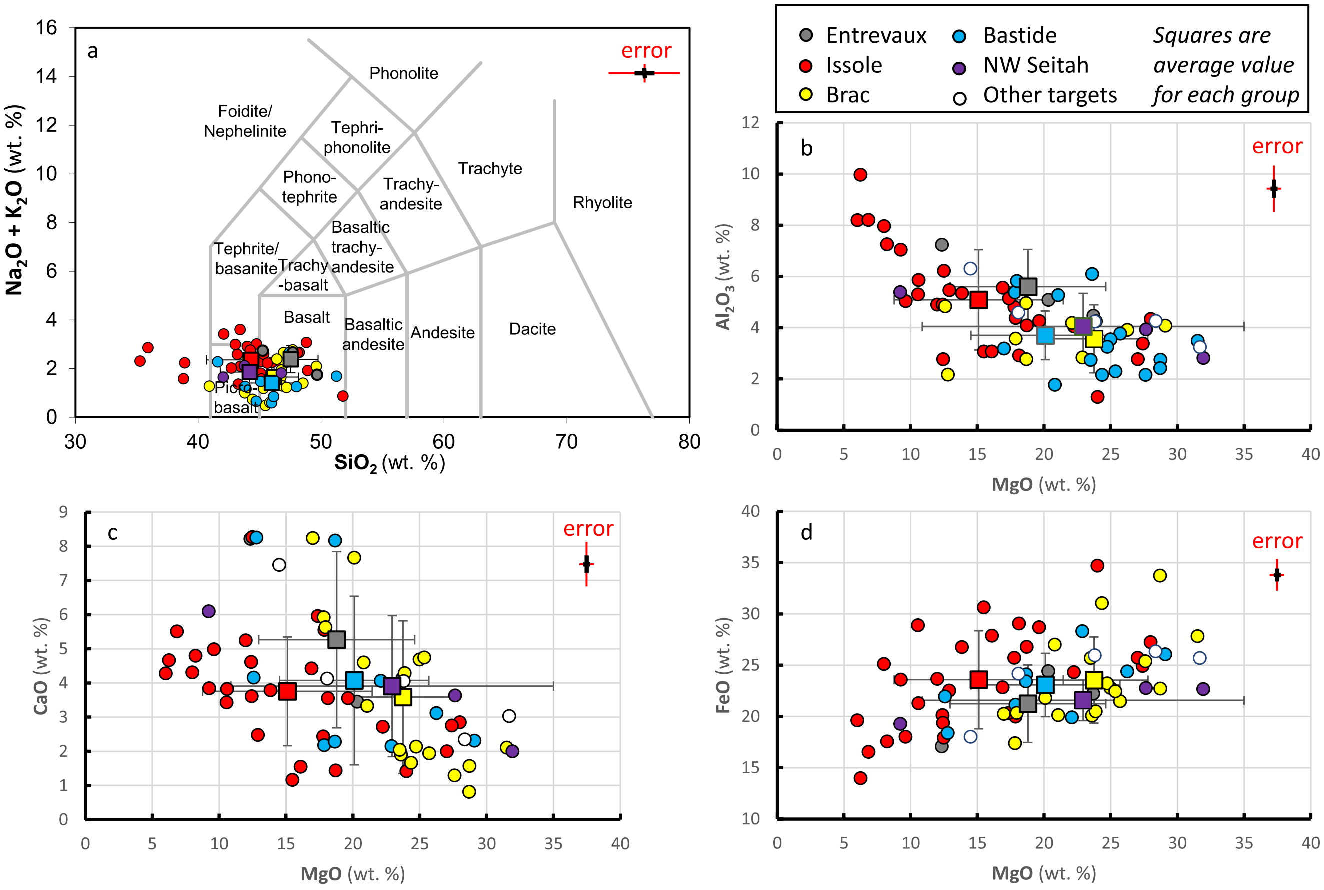

Figure 6. Major element compositions (in wt.%) for Séítah for each target (circles) and average value with standard deviation for each group as defined in the text (squares, Table 1). The color code is the same for all figures. (a) Total alkali-silica diagram, $Na_2O + K_2O$ versus SiO_2; (b) Al_2O_3 versus MgO; (c) CaO versus MgO; and (d) FeO versus MgO. Error indicated in red is the accuracy and in black is the precision for Laser-Induced Breakdown Spectroscopy, see text for more details.

(PMIDN) on Mars has a slightly higher Al/Si in the 0.09–0.14 range compared with the laboratory value of 0.07, and (Fe + Mg)/Si in the range 0.44–0.53 similar to 0.52 in the laboratory. Enstatite standard (PMIEN) on Mars has Al/Si in the range 0.01–0.06 compared to the laboratory value of 0.00, and (Fe + Mg)/Si in the range 0.88–1.12 compared to 1.01 in the laboratory. Ferrosilite standard (PMIFS) on Mars has Al/Si in the range 0.01–0.06 compared to the laboratory value of 0.03, and (Fe + Mg)/Si in the range 0.93–1.15 compared to 1.08 in the laboratory. Olivine standard (PMIFA) on Mars has a slightly higher Al/Si in the range 0.01–0.08 compared with the laboratory value of 0.00, and (Fe + Mg)/Si in the range 1.47–1.81 lower compared to 1.88 in the laboratory. Such differences reflect the fact that the LIBS elemental calibration has not been fully optimized, in particular the spectral library used for LIBS MOC calibration was not sufficiently representative of the compositions encountered at Jezero, for example, high MgO and FeOT (Anderson et al., 2022; Wiens et al., 2022). For instance, in the case of the olivine PMIFA standard, the difference in (Fe + Mg)/Si likely reflects an underestimation of FeOT and an overestimation of SiO_2 by SuperCam on Mars. The slight underestimation of FeOT translates also in Fo# of measurements on Mars, an average of 67 ± 3 for olivine PMIFA, slightly higher than the laboratory value of 64. However, note that the biases shown by the calibration targets are generally within the stated (1-sigma) accuracy of the technique. LIBS elemental calibration work is still ongoing, and the collection of additional spectra in the laboratory with laboratory analog instruments will improve the current calibration. As mentioned earlier, the precision of the MOC is better than its accuracy; consequently, we can rely on the comparison with standards in situ on Mars for mineral identification. As a consequence, all these biases have not been corrected for the Mars data, even in the next section for the stoichiometric analyses.

The data from the Séitah formation are nearly all clustered between the andesine - low- and high- Ca pyroxene—olivine endmembers (Figure 7). At first glance, Issole covers this entire domain and it is the group with the highest number of points trending toward the andesine endmember. On the other hand, Brac has a few points trending toward andesine but has the highest number of points trending toward the olivine endmember. Other groups,

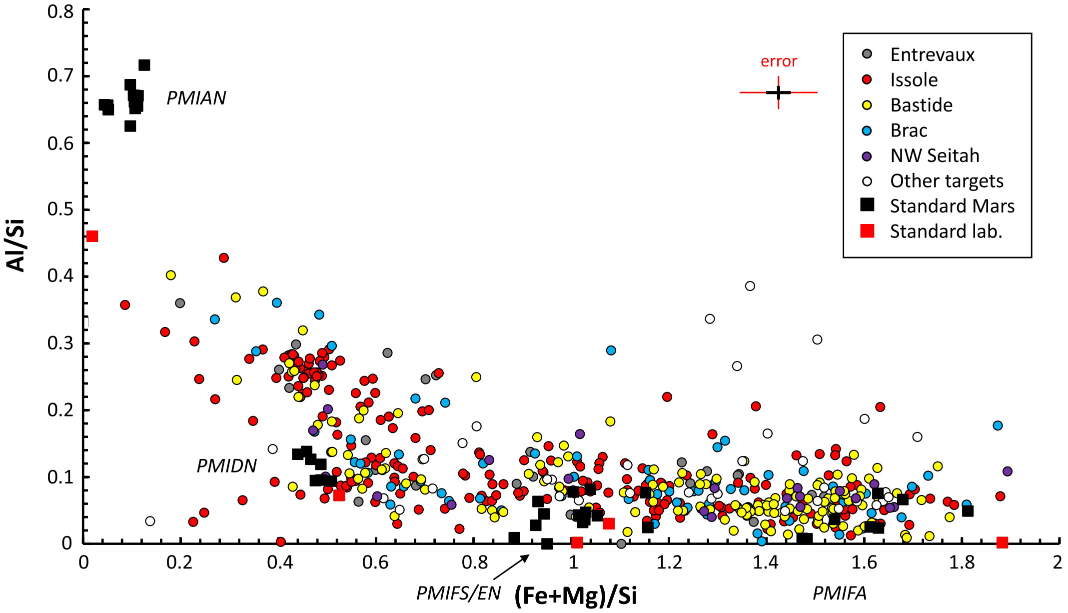

Figure 7. Molar Al/Si versus (Fe + Mg)/Si diagram for Séítah. Each point represents a single Laser-Induced Breakdown Spectroscopy (LIBS) point analysis with color code indicating the group as defined in the text. Squares represent values obtained for the standards on Mars (black, until sol 450) and by Laser Ablation Inductively coupled Plasma Mass Spectrometer in the laboratory (red). Standards are PMIAN (andesine), PMIOR (orthoclase), PMIDN (diopside), PMIFS (ferrosilite), PMIEN (enstatite), and PMIFA (olivine). Error indicated in red is the accuracy and in black is the precision for LIBS, see text for more details.

Entrevaux, Bastide, NW Séítah or isolated target. also cover the entire domain with most points scattered in the olivine/pyroxene region. This figure also emphasizes that Al, Fe, and Si are detected in all targets, whether natural rocks or the calibration targets, which were prepared from natural crystals likely not representing the perfect ideal stoichiometry (Cousin et al., 2022), or that there is contamination at low level from dust on Mars. This is also the case for Ca and Na detected in almost all points, while K and Ti are not detected in many points. Note lastly that many points are very close to the standards and may therefore represent analyses of single crystals.

5.4. Mineralogy Based on LIBS

The average millimetric grain size of the Séítah rocks is significantly larger than the LIBS spot size (∼220 μm at 3 m). In most silicate and oxide phases, the ablation depth of SuperCam LIBS is on the order of tens of μm (Chide et al., 2019, 2020). This means that the LIBS ablation may target and stay within single crystals during the whole laser burst. A fundamental way to illustrate this is to compare the LIBS spectra of the martian targets with the spectra of the onboard calibration targets. Figure 8 presents the LIBS spectrum of olivine PMIFA standard along with shot-to-shot spectra and average spectrum of Pierlas point #9 in the UV spectral range where relevant Fe, Mg, and Si emission lines occur. The five first shots are slightly different in terms of signal for Si, Mg, and Fe, but are assumed to contain a record of surficial dust or weathering products (Lasue et al., 2018), and are removed for the MOC calibration. There is a remarkable similarity between the spectra for the next 25 shots and that of PMIFA: all emission lines from Si, Fe, and Mg observed in the Martian rock can be superimposed with high confidence onto the standard spectrum. There are only some subtle variations in the relative intensities that may reflect slightly different Mg/Fe ratios between the standard and the Martian target. In addition, some weak emission lines from other elements detected in the Martian rocks are observed in the calibration target spectrum, such as Al or Ca. Figure S1 in Supporting Information S1 shows that derived MOC abundances for nearly all shots cluster very close to the PMIFA standard in the Si + Al—Fe + Mg—Ca + Na + K ternary diagram. A similar comparison can be achieved by comparing the spectrum from the PMIFS, PMIEN or PMIDS standards with spectra from some selected Martian targets, showing that some martian LIBS spectra are consistent with single clino- or ortho-pyroxene grains, with the exception that the Mg/Fe ratios differ somewhat on Mars from those of the onboard standards.

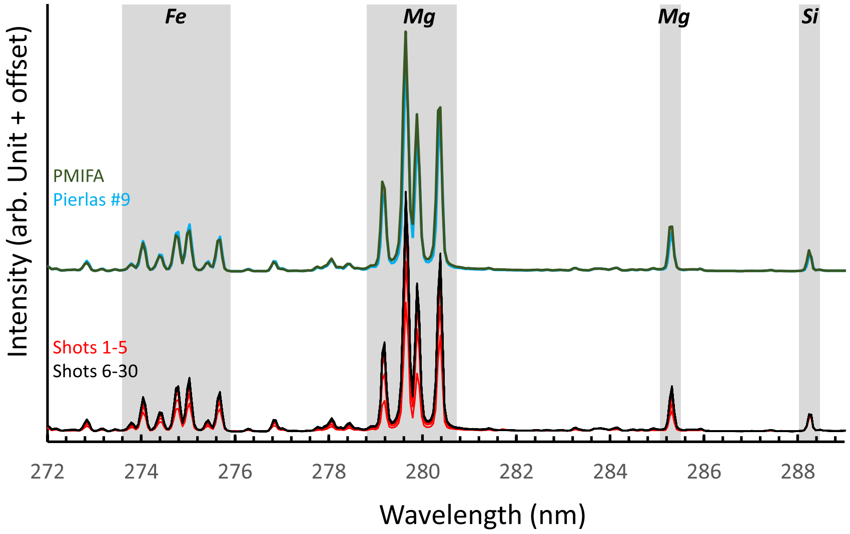

Figure 8. Laser-Induced Breakdown Spectroscopy spectra (normalized and offset) in the range 272–289 nm for the standard olivine PMIFA (sol 442) compared to target Pierlas point #9 (natural surface, Brac group, sol 252). In this spectral range, relevant emission lines for Fe, Mg, and Si are indicated. *Bottom*. shot-to-shot spectra for Pierlas #9, the first 5 spectra corresponding to dust are in red and 25 next corresponding to the rock are in black. *Top*. spectrum for PMIFA (10 shots) in green and Pierlas #9 (25 last shots) in blue. Note the excellent superposition between the spectra for PMIFA and Pierlas #9. The corresponding major-element oxide compositions composition for shot-to-shot data is depicted in Figure S1 in Supporting Information S1. See text for discussion.

Filtering all the LIBS data obtained in Séítah using the criteria listed in Table S3, we were able to isolate 60 and 45 points that have MOC compositions consistent with single olivine or pyroxene, respectively. Some representative compositions of olivine and pyroxene are given in Table 2. Olivine has been found all along the traverse in Séítah. Only one pure olivine analysis is found in the Entrevaux group, but the three targets Entrevaux, Aiguines, and Chaudon have many points with MOC compositions very close to olivine. NW Séítah targets appear rich in olivine and some have several points of pure olivine. More generally, the rocks are intrinsically heterogeneous at the outcrop scale: for instance, in the 10 × 1 raster of Dourbes, sol 268, seven points are consistent with olivine, whereas other rasters on the same abraded patch do not show pure olivine, except one point in Dourbes sol 270. The best Raman signature for olivine is obtained on the Garde abraded patch (see Section 5.5), where only one LIBS point out of 22 is consistent with pure olivine, although many points are very close to fitting the criteria for pure olivine. Martian olivines all have high LIBS MOC totals above 100 and up to 123 wt%, compared to totals in the range 96%–108% for the olivine PMIFA standard. This difference might reflect an excess of SiO_2 in the Martian analyses as well as the potential detection of elements such as Al_2O_3, CaO or Na_2O despite the strict selection criteria of Table S3. The non-zero abundances of these elements may be spurious, contributing to the high totals. Because such high totals are specifically observed for olivines and not for other mineral phases, there might be a matrix effect with the ablation and plasma generation for this mineral. Such possible matrix effects may not be observed on the olivine PMIFA standard as this target is not a single crystal but a ceramic synthetically produced from flash sintering of natural olivine powder (Cousin et al., 2022; Montagnac et al., 2018).

Through Séitah, olivine Fo# is relatively well clustered with all data in the range 54–73 (Figure 9a), except two olivine grains with Fo# of 47 in target Castiglione sol 287. In the Dourbes abraded patch, the Fo# of olivine falls in the range 58–63, in good agreement with the Fo# of 59–63 obtained from Raman spectra (see next section). However, these values are slightly higher than the average Fo# of 55 for this patch obtained by the PIXL instrument (Liu et al., 2022). As emphasized above, comparison of Mars and laboratory data for standard olivine suggests that the current MOC model slightly underestimates Fe on Mars, leading to a slight overestimation of Fo# by ~3 units, but this does not account for all the difference between SuperCam and PIXL data. On the other hand, PIXL has stated accuracy of ±10% relative for element oxides with >10 wt% abundances, although the precision of the analyses is likely better (Table S2 in Liu et al., 2022). Thereby, given the uncertainties for the two instruments, the olivine Fo# is consistent between PIXL and SuperCam as they overlap within error.

Table 2
Representative Mineral Compositions From Laser-Induced Breakdown Spectroscopy for Olivine and Pyroxene

Mineral	Target	SiO_2	*Stdev*	TiO_2	*Stdev*	Al_2O_3	*Stdev*	FeOT	*Stdev*	MgO	*Stdev*	CaO	*Stdev*	Na_2O	*Stdev*	K_2O	*Stdev*	Total	Al/Si	(Fe + Mg)/Si	Mg#
Olivine	Lioux #2	47.06	*3.79*	0.01	*0.01*	3.41	*1.04*	29.77	*2.32*	36.88	*3.71*	1.23	*0.51*	0.41	*0.11*	0	*0.3*	118.77	0.09	1.70	69
Olivine	Dourbes268 #4	42.24	*2.22*	0.01	*0*	2.35	*1*	35.68	*4.52*	28.64	*1.49*	0.57	*0.19*	0.37	*0.14*	0	*0*	109.86	0.07	1.72	59
Olivine	Pierlas #5	42.69	*2.33*	0.01	*0*	1.44	*0.85*	37.02	*3.12*	30.05	*1.03*	1.14	*0.41*	0.55	*0.13*	0	*0.2*	112.9	0.04	1.77	59

Mineral	Target	SiO_2	*Stdev*	TiO_2	*Stdev*	Al_2O_3	*Stdev*	FeOT	*Stdev*	MgO	*Stdev*	CaO	*Stdev*	Na_2O	*Stdev*	K2O	*Stdev*	Total	Al/Si	(Ca + Fe + Mg)/Si	Mg#	Wo	Fs	En
Pyroxene	Amen #6	47.09	*1.38*	0.04	*0*	0.89	*0.82*	20.27	*1.75*	12.98	*0.84*	9.87	*0.78*	0.7	*0.13*	0	*0.1*	91.84	0.02	1.00	53	23	36	41
Pyroxene	Castellet #9	46.84	*2.19*	0.04	*0.09*	1.89	*1.25*	21.79	*1.52*	14.81	*1.16*	7.9	*1.18*	0.84	*0.2*	0	*0.01*	94.11	0.05	1.04	55	17	37	45
Pyroxene	Garde_209a #3	44.48	*1.73*	0.01	*0*	2.86	*1.43*	26.9	*4.22*	14.94	*2.39*	0.52	*0.34*	0.82	*0.17*	0	*0.08*	90.53	0.08	1.02	50	1	50	49
Pyroxene	Pal #1	45.37	*3.77*	0.05	*0.03*	3.24	*1.71*	20.12	*1.38*	18.38	*4.19*	1.39	*0.76*	0.47	*0.19*	0	*0.01*	89.02	0.08	1.01	62	3	37	60

Note. See text for details on precision and accuracy of chemical quantification from LIBS data.

Figure 9b shows a pyroxene diagram consisting of SuperCam data from Séítah. There are two groups of pyroxenes: (a) high Ca-pyroxene (clinopyroxene) with Wo > 17 (27 grains) and composition in the range $Wo_{17–41}Fs_{18–40}En_{34–46}$, and (b) low-Ca-pyroxene (clino- and ortho- pyroxene) with Wo < 10 (18 grains) and composition in the range $Wo_{1–9}Fs_{30–54}En_{39–67}$. All pyroxene analyzed by SuperCam contain Ca, but some points have very low Ca content, and are close to the enstatite-ferrosilite join, such as point #3 of Garde_209a. Totals are highly variable with values in the 88–108 wt.% range for the pigeonite and 82–97 wt.% for the augite. This is in agreement with data for the standards, as the diopside PMIDN target has low totals in the range 81–84 wt.%, while the enstatite PMIEN and ferrosilite PMIFS have higher totals in the range 95–102 and 88–99 wt.%, respectively. The Mg# is variable in the pyroxenes: pigeonites have Mg#s in the 41 to 68 range with all but two points below 60, while augite Mg#s fall in the range 48–71 with all but four points above 55. Similar to olivine, the two types of pyroxenes were found all along the traverse except in NW Séítah. However, we have substantially less data for the NW Séítah region, and some MOC compositions for NW Séítah are very close to pyroxene suggesting that these rocks contain pyroxene as well.

LIBS has the capacity to detect many other elements including minor and light elements. For instance, the Séítah rocks contain some C, most likely in carbonate phases (Clavé et al., 2022), S in sulfate phases and Cl in perchlorate phases (Wiens et al., 2022), each of which is related to fluid-rock interactions and alteration of these rocks. In the stoichiometric analysis of olivine and pyroxene, we also set an upper limit for the H score (Figure S2 in Supporting Information S1), which is a term used to represent the area of the H band within each LIBS spectrum. A few points with a major element composition consistent with that of olivine and pyroxene actually exhibited a relatively high H score and were therefore removed from our analysis. This may correspond to H-bearing mineral phases to be identified and/or may suggest that olivine and pyroxene phases may locally be intimately mixed with or coated by an H-bearing mineral phase. Using the same approach, we also checked to see whether olivine and pyroxene phases within Séítah are associated with enrichment of Mn or Cr. LIBS detection limits for these elements are variable, from about 120 for Cr (Anderson et al., 2023) to 300 ppm for Mn (Gasda et al., 2021). In general, Séítah rocks are less rich in Mn compared with some rocks of the Máaz formation, and we did not observe any significant Mn enrichment within olivine and pyroxene phases, although the Séítah rocks may contain some Mn. Some points are very rich in Cr (see below), but we did not detect any significant enrichment or depletion of Cr for the pure olivine and pyroxene phases.

Other minerals also appear to be present in these rocks but were not probed as pure phases by LIBS. In Figure 7, some points are clearly trending toward the plagioclase endmember and thus likely represent a mineral mixture in which plagioclase is dominant. Such points are depicted in the ternary diagrams of Figure S3 in Supporting Information S1 and were found mostly in the Entrevaux and Issole groups (Table S2). They are closer to the Na-rich (albite) endmember rather than the Ca-rich (anorthite) endmember in terms of chemical composition. Many other points may contain some plagioclase mixed, for instance, with pyroxene and/or olivine, but plagioclase appears as a minor, likely fine-grained component. Some accessory minerals are also present in these rocks, such as phosphates and Fe-Ti-Cr oxide phases. Phosphate phases are detected by LIBS through the P emission lines. In some cases, the CaF molecular emission (Forni et al., 2015) is also detected, and is correlated with P lines in the shot-to-shot data, allowing the identification of fluorapatite. These phosphates are not detected in the Raman data, most probably owing to grain size that is too small, but the presence of CaF lines supports the presence of apatite rather than merrillite. All along the traverse, some points exhibit a strong Cr emission line, often associated with high FeOT content, and to a lesser degree, high TiO_2 contents. Some points have a very strong Cr line, suggesting the presence of a Cr-rich mineral phase that could be chromite, a common mineral in olivine-bearing Martian meteorites, or Cr-rich magnetite. The presence of Ti in the spectra makes the presence of Cr-rich ulvöspinel also plausible. Finally, a few points are very rich in FeOT and a few others in TiO_2, which likely reflect the presence of Fe-oxide phases such as magnetite or hematite, and/or Ti-oxide phases such as rutile, and/or Fe-Ti-oxide phases such as ilmenite, in these rocks. At the spatial resolution of SuperCam LIBS, it is impossible to resolve further the precise mineralogy and chemistry of these minor minerals. Note that these minerals were not detected by Raman and VISIR spectroscopy as they may be too small compared with the analytical footprint of these techniques and/or because they have a weak spectral response for VISIR or Raman (oxides generally). The small size of these accessory minerals is confirmed from the PIXL analysis of Dourbes (Liu et al., 2022).

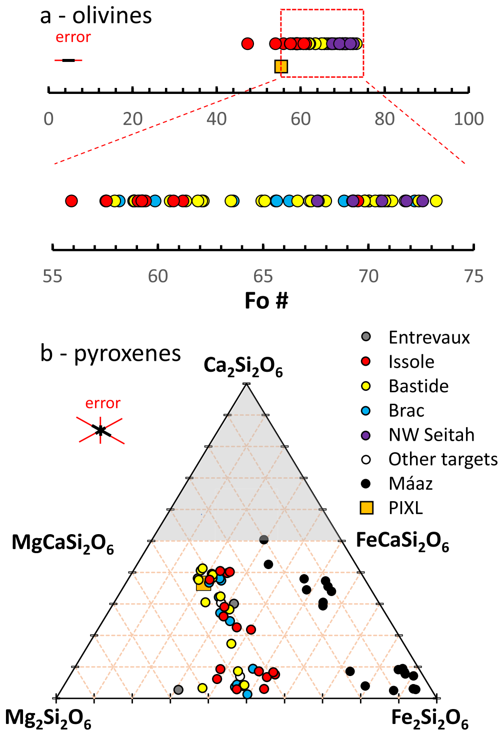

Figure 9. Composition of olivines and pyroxenes. (a) Fo# = Mg/(Fe + Mg) for olivines in Séítah. Each point represent a Laser-Induced Breakdown Spectroscopy (LIBS) point with composition consistent with olivine following criteria defined in Table S3, color code indicated in panel (b). (a) Ternary diagram for pyroxenes in Séítah (color indicates group) with two main populations: low-Ca (Wo < 10) and high-Ca (Wo > 10) pyroxenes. Planetary Instrument for X-ray Lithochemistry composition for pyroxene in Dourbes is indicated (Liu et al., 2022) as well as SuperCam pyroxene compositions for the Máaz unit (Udry et al., 2022). Error indicated in red is the accuracy and in black is the precision for LIBS, calculated at the center for ternary diagram, see text for more details.

5.5. Mineral Detections Based on Raman and VISIR Spectroscopy

Here, we describe the detection of primary minerals by VISIR and Raman, in particular olivine, the dominant mineral in Séítah. A detailed description of the VISIR data of the crater floor, including secondary alteration phases, is given by Mandon et al. (2022). Note that both VISIR and Raman spectroscopy have relatively large footprints compared with LIBS and generally analyze mineral mixtures instead of single crystals.

Olivine was first detected using VISIR spectroscopy and LIBS in the coarse-grained regolith covering the Máaz formation, and then by long-distance VISIR spectroscopy targeting Séítah while the rover was still in Máaz (Figure 4). Figure 10 depicts some representative VISIR spectra from the rover workspace that are all consistent with the presence of olivine. Olivine displays a strong and characteristic VISIR signature consisting of a broad band centered at ∼1 μm due to the presence of ferrous iron crystal field transitions. The position and shape of this band depend on many parameters including the grain size, the olivine Fo# and/or the presence of mineral mixtures (e.g., Ody et al., 2013), which limits the use of these spectra to estimate olivine Fo#. In the SuperCam VISIR spectra, the center of the band lies within a gap between the VIS and IR regions of the spectra. The presence of olivine, however, is confirmed by a strong red slope from 1.3 to 1.8 μm including a clear downturn at about 1.5 μm on the near IR side. On the VIS side, the slope decreases from about 0.7 μm to the upper limit of the range at about 0.85 μm. Additionally, in the near IR region, spectra are occasionally nearly flat at higher wavelength or, more commonly, with a decreasing reflectance from 1.8 to 2.6 μm, suggestive of the presence of a hydrated phase. In addition, several bands due to hydration such as at ∼1.94 μm, or hydroxylation such as at 2.23, 2.29, 2.33 or 2.39 μm are commonly observed. Such bands likely reflect cation-OH bond vibrations in other minor phases such as phyllosilicates, which are often observed in these rocks (Mandon et al., 2022). Locally, carbonate phases that have been detected may contribute to the 2.33 μm bands (Clavé et al., 2022).

VISIR spectral signatures of pyroxene are also present in the rocks of the Séítah formation. Pyroxene signatures are dominated by two large bands centered at about 1 and 2 μm, but their position varies with the Ca, Fe, and Mg contents of the pyroxene for a given grain size (Adams, 1974; Cloutis & Gaffey, 1991; Klima et al., 2011; Skok et al., 2010). High-Ca pyroxene has a positive slope from 1.3 to 1.8 μm while this slope is negative for low-Ca pyroxene. All pyroxene phases show a decreasing slope at wavelength higher than 2.1 μm. In olivine-pyroxene mixtures, the olivine signature generally dominates. To track low-Ca pyroxenes, the IR slope at 1.6 μm for all spectra was projected on a ternary Si-Mg-Fe diagram. High values for this slope are characteristic of olivine but are also observed for some spectra present in the region of orthopyroxene in the ternary diagram. These IR spectra were then divided by the average reference spectrum of olivine to substract the olivine contribution (see Forni et al. (2023) for the methodology). For several targets, the remaining spectra exhibit a slope in the range 1.3–1.8 μm which is clearly negative, hence indicating the presence of low-Ca pyroxene mixed with olivine (Figure S4 in Supporting Information S1). Plagioclase is not detected by VISIR as this mineral has weak spectral signature with this technique.

Raman spectroscopy has been used at various localities on natural surfaces as well as systematically on the abraded patches (Figure 11). Most Raman spectra of Séítah targets display a band, often composed of two visible

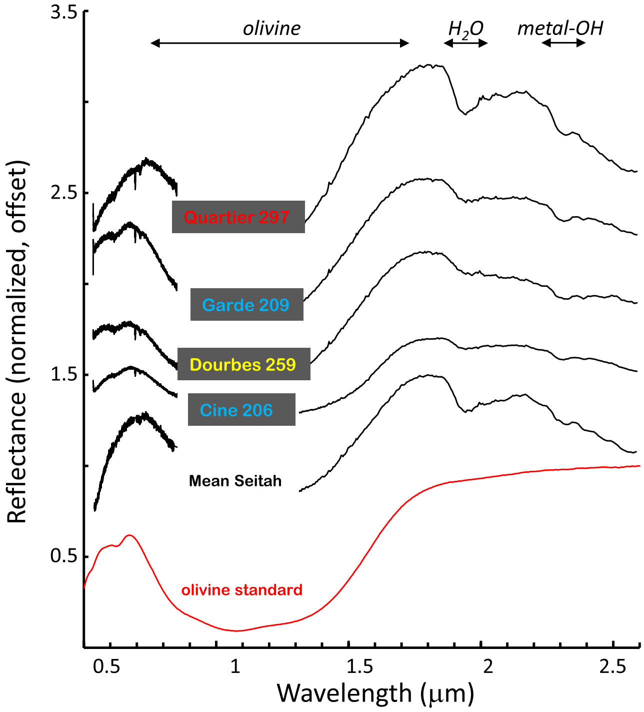

Figure 10. Supercam Visible and Infrared reflectance spectra (normalized, offset) for Séítah compared to a reference spectrum of olivine (RELAB C1PO47). Spectra for Quartier 297, Garde 209, and Dourbes 259 were obtained on abraded patches, while spectrum Cine was obtained on a dust-free natural surface. The mean spectrum for Séitah is represented (Mandon et al., 2022). All spectra exhibit a strong absorption band at ∼1 µm indicative of olivine similar to the reference spectrum as well as a hydration band at ∼1.9 µm and a band at ∼2.3 µm due to metal-OH absorption, likely Mg-OH.

peaks, located in the range 810–850 cm^{-1}. The best candidate is olivine, for which a complete description of the Raman spectrum is given by Kuebler et al. (2006) and references therein. In the olivine Raman spectrum, the most intense feature occurs as a doublet with peaks around 820 and 850 cm^{-1} with relative intensities varying with crystal orientation. This characteristic doublet is classically used to identify olivine and results from internal stretching vibrational modes of the SiO_4 ionic group. Interestingly, the positions of these two peaks also vary with the Fo#. Specifically, there is a systematic increase of peak position with increasing Fo# due to the decrease in both atomic mass and in the volume of octahedral sites that result from substituting Fe by Mg, in combination with the degree of coupling of the symmetric and asymmetric stretching vibrational modes of SiO_4. Peaks <400 cm^{-1} are generally weak and assigned to lattice vibration modes including rotational and translational motions of SiO_4 as a unit, and translational motions of octahedral cations (Mg^{2+}, Fe^{2+}) in the crystal lattice.

Average spectra obtained through complete rasters instead of spectra from single points are discussed for Martian targets because (a) a higher number of laser shots improve the SNR and (b) the analytical footprint of Raman is generally larger than the grain-size. For some rasters, however, spectra with lowest SNR were not included in the average spectrum. Data with the highest SNR were collected on the Garde abraded patch. Garde 207a and Garde 209a exhibit a nice doublet with peaks at ∼818/848 and ∼819/849 cm^{-1} respectively, which are consistent with olivine. No other peaks are detected such as hydration or hydroxylation features in the range 3,400–3,600 cm^{-1}. In the other spectra, either from natural surfaces (Penne sol 211) or abraded patches (Dourbes sol 259, Quartier sol 295), the doublet is not as obvious. Instead, a wide band is observed in this spectral range. This might be due to a combination of instrumental factors such as the relatively low spectral resolution of SuperCam. Also, it can be possibly due to the physical properties of the targets, which generally consist of a mixture of grains of various sizes, are dusty and have a rough surface, which are all detrimental aspects for Raman analysis. Fitting the spectra Garde 207a and 209a yields Fo# of ∼59 and ∼63, respectively, using the Fo(DB2) calibration valid for Mg-rich olivine by Kuebler et al. (2006). Note that this represents an average Fo# for the olivine grains, as the analytical footprint is larger than the grain size and several points are included to build the spectra. For Dourbes sols 259 and 268 spectra, which have high SNR and for which the two peaks are barely distinguishable, we obtain Fo#s of 63 and 59. Extracting this data for the other spectra is challenging because of their low SNR and/or the difficulty to separate the two peaks in the Raman signal. Noticeably, the Raman contribution of olivine is much weaker in all spectra from the Quartier abraded patch compared to Dourbes and Garde. In addition, although pyroxene is detected by LIBS, Raman did not detect any characteristic peaks of pyroxene in any Séítah target. This might reflect the lower Raman efficiency and higher optical absorption, and/or possible smaller grain size and lower abundance, of pyroxene compared to olivine in these rocks.

5.6. Modal Mineralogy of Séítah Formation

Modal mineralogy of the Séítah rocks has been estimated using two approaches: CIPW norms based on LIBS chemical data and spectral modeling of the IR spectra. In both cases, this is a challenging exercise, strongly model-dependent and relying on assumptions, but this provides a first quantitative constraint on the mineralogy of these rocks.

CIPW norms have been developed to infer modal mineralogy from elemental compositions of magmatic rocks. Because CIPW norms do not deal with secondary alteration phases, we exclude LIBS points with low totals (<80 wt%), assuming that low totals are linked to alteration phases. However, we cannot exclude that such phases may contribute as mixtures to some points kept in our data set. Another limitation of the approach is that our current MOC quantification does not include some elements such as Mn, P, Zr, Cr, or S, which may be important

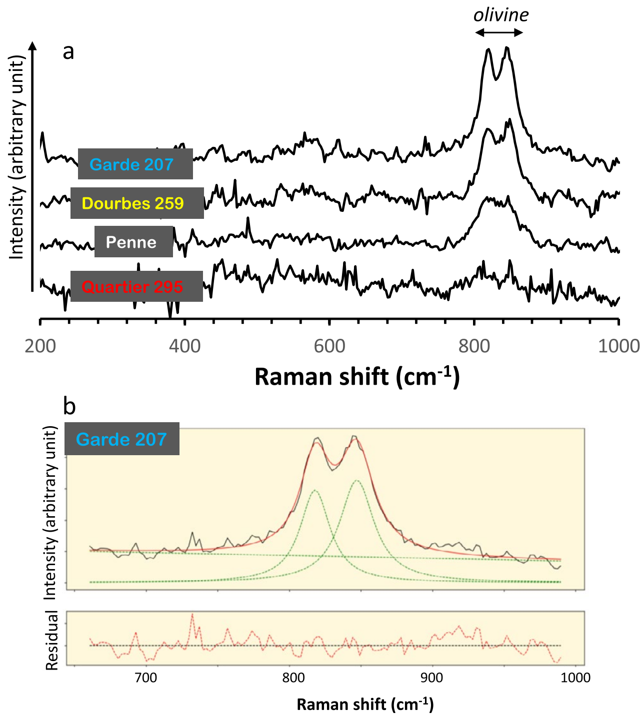

Figure 11. (a) Representative Raman spectra obtained in Séítah. All spectra are raw data with just Raman contribution from the MU-BU optical fiber removed (see text). Spectra for Quartier 295, Garde 207, and Dourbes 259 were obtained on abraded patches, while spectrum Penne was obtained on a dust-free natural surface. All spectra show a Raman signal in the range 810–850 cm^{-1} weaker in Quartier 295. Note that the characteristic doublet for olivine is nicely observed in spectra from Dourbes 259 and Garde 207. (b) Example of peak fitting (linear baseline, Voigt profile for peaks) of the olivine doublet yielding two peaks at ~818 and ~848 cm^{-1}.

in the constitution of some minerals, for example, phosphates, Cr-rich oxides or sulfides. All this explains why the totals for the bulk composition of rocks are below 100%. Methodologically, each LIBS analysis samples a volume of rock which is well below 1 mm^3. To obtain the best representativity in Séítah rocks, which have a relatively large grain size (mm-scale), we decided to run CIPW norms on average data from several rasters of the same group. We did that only for the Issole, Bastide, and Brac groups for which we have a large number of rasters and of LIBS analyses (Table 1). Here, CIPW norms are used as a first-order insight into the modal mineralogy of these rocks and also as an indication of possible variability among these three groups. For the CIPW norms, we use the approach by Hollocher (2004). Because the totals are close to 100 wt%, the chemical data were not normalized before running the CIPW calculation. Tests show that normalization to 100 wt% would change the respective proportions by only a few percent, generally below 5%. Another important parameter is the Fe^{2+}/Fe^{3+} ratio that we do not know for Séítah rocks. Because some Fe-oxides are present in these rocks, we cannot rule out the presence of some Fe^{3+} in the bulk composition in the form of hematite, for instance. In addition, ferrihydrite has been potentially detected by NIR in some rocks, but constraining the respective abundance of such phases from reflectance spectra is highly uncertain (e.g., Sherman & Waite, 1985). We tested two compositions: one with all FeOT as Fe^{2+} and one with 5 wt% of FeOT as Fe_2O_3. No significant difference was observed between these two compositions. Results of CIPW norms are provided as wt% (Table 3).

In addition to the CIPW approach, spectral modeling of IR spectra can provide insights in the modal mineralogy. Such a methodology has already been applied to orbital (Poulet et al., 2009) and in situ data (Lapotre et al., 2017). It consists of the simulation of the scattering properties of a mineral mixture and is based on the radiative transfer theory in a compact medium. For this, a model input consisting of an intimate mixture of pure minerals with reference laboratory spectra is tested against the Mars IRS data using a best fit procedure (Poulet et al., 2009). Here, we restrict the application of this approach to abraded sulfate-free IRS data. This approach also requires assumptions concerning the medium, including the grain size and the mineral phases present (see Poulet et al. (2022) for more details). It is important to remind that NIR spectroscopy is very sensitive to hydrated phases or molecular bonds like C-O but is only weakly sensitive to some primary phases like plagioclase. Among the primary phases, olivine has the strongest and most charac-

Table 3
CIPW Normative Modal Abundances Compared to Mineral Abundances Determined by Non Linear Modeling of IR Data From Abraded Patches of Dourbes and Garde (Results for the Dourbes Tailing Are Also Listed)

	LIBS CIPW (vol%)			IRS modeling (vol%)		
	Bastide	*Brac*	*Issole*	*Séítah*		*Dourbes tailings IRS*
Olivine	41.2	54.3	40.7	30–50		67 ± 11
Pyroxene (all)	38.5	25.6	28.5	10–35 (augite)		10 ± 5
Plagioclase/feldspars	20.0	19.9	30.5	<10		–
Mg-serpentines	N/A	N/A	N/A	Up to 20	35–50 (in total)	<5
Smectites (Fe and Mg)	N/A	N/A	N/A	Up to 20		<5
Carbonates	N/A	N/A	N/A	Up to 20 (Fe-)		9 ± 6
Fe-Ti-oxide/hydroxide	0.3	0.2	0.3	Up to 10		–

Note. Here, the CIPW results presented are obtained with all FeOT as Fe^{2+}, the results with 5% Fe^{3+} are not significantly different (see text). The rocks compositions for each group are listed in Table 1.

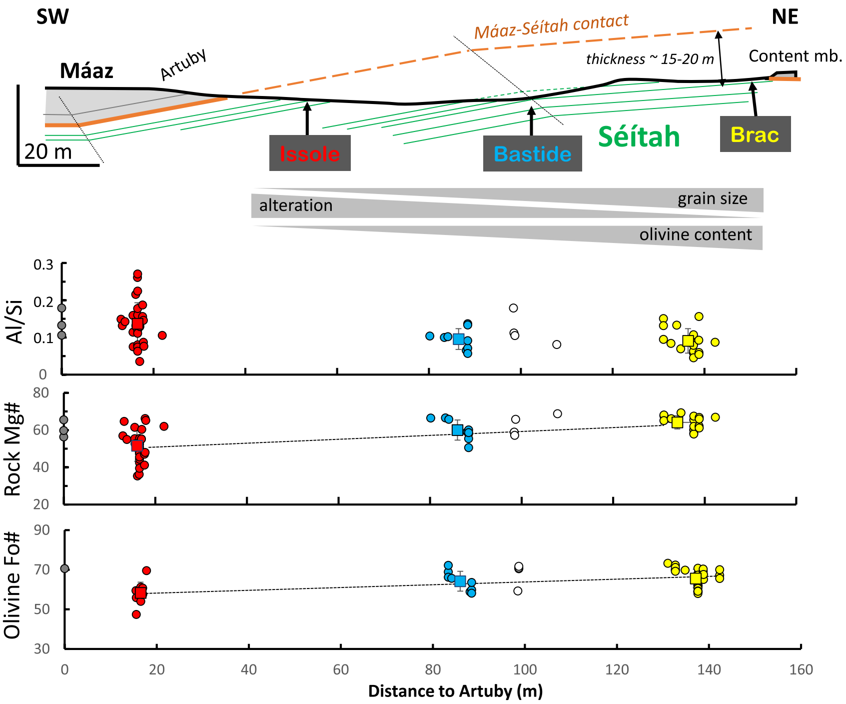

Figure 12. Summary of SuperCam observations along the rover traverse in SE Séítah. The top cross-section is located in Figure 1. Olivine Fo#, bulk rock Mg#, and Al/Si molar ratio (Table 1) are represented for each target (circles) and average value for the group with standard deviation (squares). Mg# = Mg/(Fe + Mg). Red is Issole, yellow is Brac, and blue is Bastide. The qualitative overall trend for grain size, olivine content, and alteration is also indicated (see text).

teristic signature. One strong advantage of IRS is that the analytical footprint is much larger than the LIBS spot size as it covers surfaces of several mm^2 and generally samples mineral mixtures making the assessment of bulk mineralogy more representative. Results are provided as vol.%.

Results from the two approaches are presented in Table 3. At first glance, there is a quite good agreement on olivine (here assuming olivine Fo# of 40 for IR modeling), and pyroxene being the two dominant phases with the most abundant being olivine in all cases. Regarding olivine, the IR modeling returns a much larger value at the expense of the hydrated phases compared with that for the associated tailings data for Dourbes. This contrasting mineral assemblage could reflect mixing effects resulting from the abrasion process and/or grain sizes that are not properly accounted for within the tailings. In addition, LIBS predicts more pyroxene compared to IR modeling, especially for the Bastide abraded patch. From IR modeling, Quartier seems to be more altered than the two other patches, which is consistent with the fact that LIBS targets from the Issole group show the highest density of LIBS analyses with low totals likely corresponding to secondary minerals. Comparison of our CIPW modal mineralogy with PIXL results (Liu et al., 2022) is instructive. For the Dourbes abraded patch, PIXL estimates are ~65, 13, and 10 vol.% for olivine, pyroxene, and mesostase (including plagioclase), respectively, where SuperCam estimates are ~66, 26, and 13 vol.%, respectively. For the Garde abraded patch, PIXL estimates are ~57–65, 8, and 26–34 vol.% for olivine (including alteration phases texturally associated with olivine), pyroxene, mesostase (including plagioclase) where SuperCam estimates are ~44, 39, and 14 vol. %, respectively. Differences may arise from (a) heterogeneities in the rocks, PIXL analyzes one single patch while SuperCam analyzes several rocks in the workspace and (b) the methods themselves, as we compare an analysis of scan images for PIXL with CIPW norm models for SuperCam.

6. Discussion

Here, we review the SuperCam data obtained for the Séítah formation and discuss them in light of existing literature, including recent work and articles by the Mars2020 team. In the future, and given the mission objectives (Farley et al., 2021; Sun et al., 2023), Perseverance will likely not visit the Séítah formation again, yet it will likely visit other parts of the regional olivine-carbonates unit on the crater rim and outside the crater during the extended mission (Farley et al., 2020).

6.1. Geochemical and Mineralogical Evolution in Séítah

Figure 12 depicts a synthesis of the observations by SuperCam along the traverse into Séítah. Note that NW Séítah is not included in this figure but the three targets analyzed there show a petrology broadly consistent with that of the rocks along the traverse, with closer affinity with the Bastide and Brac groups. As described in the previous section, the Séítah formation occurs stratigraphically beneath Artuby ridge (Máaz formation) in the SW and below the Máaz formation near the Octavia E. Butler landing site to the NE. On Figure 12, we have tentatively drawn a schematic cross-section that shows changes in dip within Séítah of ∼10°–15° at Issole to ∼5° at Brac. Long-distance RMI images further show that the Séítah formation dips remain horizontal going NE into the inner regions of the Séítah exposure. Taking into account these changes in dip, Perseverance explored a thickness of about 15–20 m within the upper Séítah formation, but we have little evidence of the total thickness of the formation. The Séítah formation is stratified with an apparent increase of layer thickness going deeper in the formation toward Brac. This layering is observed consistently in all observed regions of exposed Séítah formation and does not correspond to an observable chemical or mineralogical variation at the outcrop scale. Layering is common in cumulate rocks on Earth (Holness, 2021) with two major types: dynamic layering reflecting large-scale movement of solids and liquids in a liquid-rich environment, or non-dynamic layering due to processes reflecting changes in the conditions of crystallization or self-organization in crystal-rich environments to decrease the energy of the system. In Séitah, layering is certainly magmatic, and was locally accentuated by wind erosion emphasizing the joints that form the primary layer boundaries, but we do not have clues at this stage to explain its formation.

The absence of a chemical or mineralogical control over apparent layering in the Séítah formation is broadly consistent with its hypothesized origin as an igneous cumulate deposit. The crystalline and coarse-grained texture that is typical of cumulate rocks is observed everywhere we investigated the Séítah formation, with only some change in grain size. Along the traverse, as shown by Figures 6, 7, and 9, bulk geochemistry and mineralogical composition, however, do show some variation. Séitah rocks near the Issole group are enriched in alkali elements and Al_2O_3 and depleted in MgO compared to those near Brac. This converts into an average higher Al/Si molar ratio with more variability for Issole compared to the Brac and Bastide groups. The average rock Mg# is more variable yet generally lower for the Issole group compared to inner Bastide and Brac groups. There is also a general increase of rock Mg# from Issole (∼52 ± 8) to Brac (∼64 ± 4) going deeper in the formation. This indicates that Issole has an overall different chemistry than the inner Bastide and Brac groups. Such a difference might reflect a different initial bulk composition of the source magma and/or a higher position in the stratigraphic column, hence a more differentiated composition with all rocks deriving from the same parental magma. In addition, Issole seems also more altered than Bastide and Brac as attested by the higher number of LIBS analyses with totals <80 wt.% and detections of secondary phases like carbonates (Clavé et al., 2022) or perchlorates and sulfates (Tice et al., 2022; Wiens et al., 2022). Because Issole lies relatively close to the contact with the overlying Máaz formation, we suggest that this alteration may represent either alteration during the exposure of Séitah and development of a regional unconformity between Séítah and Máaz formations, or fluid-rock interactions that may have occurred post-depositionally along this contact. Note that the Entrevaux group does not always show evidence for more alteration. However, it is composed of only three targets without an abraded patch, where the best detection of alteration phases is present, and two of these targets are likely float rocks with uncertain origin in terms of their positioning within the Séitah formation.

In terms of texture and mineralogy, Issole has slightly smaller grain size, despite all three groups containing the same dominant minerals: olivine and pyroxene. More pure olivine grains per raster were found by LIBS in the Brac group in agreement with the results of CIPW normative mineralogy. Pyroxene phases, either clino- or ortho- pyroxenes, seem evenly distributed along the traverse. The olivine Fo# shows some variability for all groups as described previously, but also shows a general systematic increase going farther into the Séítah formation: ∼58 ± 5 on average in Issole, ∼64 ± 5 in Bastide, and ∼66 ± 5 in Brac based on LIBS. This variation may result from a different composition of the parental melt from which olivine crystallized, or from crystallization along different portions of the liquid line of descent from the same parent melt, or both. In general, olivine with higher Fo# crystallizes earlier, that is, at higher temperature, suggesting that the farther interior Brac and Bastide outcrops represent more primitive stages of olivine crystallization in the magma. It could also represent the recharge of different pulses of magmas with different compositions within the magmatic chamber. The Mg#s for pyroxene are generally systematically lower than the olivine Mg#s within the same rock/group. The average Mg# of pyroxene is ∼53 ± 7 for Issole, ∼56 ± 6 for Bastide and increases to ∼62 ± 7 for Bastide, also showing a general increase when going deeper in the formation. Note that this trend of average value is not easy to interpret as it includes both clino- (augite and pigeonite) and ortho- pyroxenes. Pigeonite, being generally more ferroan than both olivine and augite, does not seem in equilibrium with these two phases and may represent a later-stage crystallization phase. Augite has been shown to envelop olivine in a poikilitic texture in Dourbes (Liu et al., 2022).

6.2. Crystallization Sequence of the Séítah Formation

The mechanism of emplacement of an olivine cumulate with large millimeter-sized olivine crystals on the Jezero crater floor remains uncertain. Liu et al. (2022) and Wiens et al. (2022) clearly established the igneous and cumulate nature of the Séítah formation based on the observations of the Dourbes abraded patch by the PIXL and SuperCam instruments. The SuperCam data set confirms the cumulate nature of the rocks in all the areas visited by Perseverance in Séítah: this is true for the southeastern and NW sides of Séítah (Figure 1), and likely in between, as dominant olivine is detected everywhere by long-distance VISIR and orbital data (e.g., Horgan et al., 2020). However, there are some subtle variations as seen by SuperCam in terms of structure, texture, bulk geochemistry, and mineralogy. These variations may reflect different parental magma for the rocks near Issole as compared to those near Brac and Bastide or within NW Séítah. Alternatively, these differences may result from various positions in a zoned magma body showing various degrees of differentiation from the same parental magma: Issole being structurally shallower has a bulk composition and mineralogy consistent with more differentiated rocks.

As locally established by Liu et al. (2022) for the Dourbes abraded patch, olivine Mg#s are similar to the whole rock Mg#s (Figure 13). This implies that olivine is not in chemical equilibrium with a liquid that has the whole rock composition, as the exchange coefficient for Fe-Mg partitioning between olivine and basaltic melt is 0.35 (Filiberto & Dasgupta, 2011) to 0.36 (Matzen et al., 2022) for Mars. This disequilibrium is a key argument for the determination of the cumulate nature of these rocks as it implies that the olivine did not crystallize in place to form the host rock, but instead is derived from an unknown melt composition. Olivine then settled by gravity in the current material before the interstitial melt between the accumulating olivine grains solidified. The SuperCam data set presented here offers the opportunity to investigate this disequilibrium all along the rover traverse. In Figure 13, for each olivine grain, the olivine Mg# is plotted against the rock Mg#, which is the average composition of the raster in which the olivine was probed. All data from Séítah are significantly above the equilibrium line even if the greatest value for the exchange parameters (Matzen et al., 2022) is taken. This confirms that olivine is not in equilibrium with the host rock in any of the regions of the Séítah formation visited by Perseverance. This may suggest that the whole of the exposed Séítah formation consists in a mafic to ultramafic cumulate.

Figure 13 also provides an insight into the Mg# of the parental magma from which the olivines crystallized. Using the curve representing the equilibrium Fe-Mg exchange parameter, samples from the Bastide and Brac regions yield a similar Mg# for the parental magma in the range 32–48. NW Séítah has a more restricted range of Mg# for the parental magma from 43 to 48, but that may be due to the lower number of olivine crystals analyzed in this group. Issole yields a wider range of Mg# for the parental magma with all but two olivine grains in the 30–36 range; including the last three grains expands the range to 24–44. The inferred Mg# for the parental magma of SuperCam olivines is higher than the value obtained by PIXL for the Dourbes abraded patch in the Brac region (Liu et al., 2022), including the Brac group to which Dourbes belongs. However, the eight olivine grains measured by SuperCam LIBS within the Dourbes abraded patch have Mg# in the range 58–63 for a bulk rock Mg# of 60, placing them closest to the PIXL data. This difference between PIXL and SuperCam may result from the different techniques and their respective calibrations and spatial resolutions. On the other hand, it also certainly reflects real chemical variability along the profile that is documented by SuperCam data, but which was not analyzed by PIXL.

More generally, SuperCam observations are in good agreement with PIXL conclusions for the Dourbes abraded patch (Liu et al., 2022), and permit expansion of these conclusions, with some variation (e.g., Issole vs. Bastide and Brac) to the whole region explored by Perseverance: Séítah is an olivine cumulate with large and homogeneous olivine crystals that likely formed by settling and enrichment of olivine through multi-stage cooling of a thick magmatic body of at least several tens of meters. In such process, there should be a counterpart region depleted in olivine, less mafic and more felsic, that is generally enriched in pyroxene, followed by enrichment in plagioclase (Holness, 2021). This

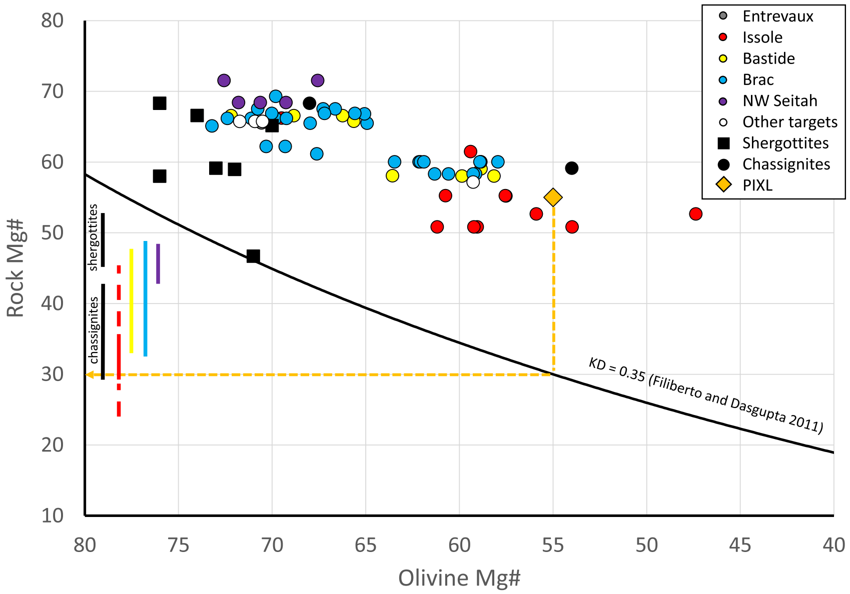

Figure 13. Comparison of olivine composition in Mg# with the bulk rock Mg#. Mg# = Mg/(Fe + Mg). Each olivine is compared to the host rock composition (target). KD is the equilibrium distribution coefficient of Fe-Mg between olivine and melt (Filiberto & Dasgupta, 2011). Dashed horizontal lines with arrows indicate the silicate melt Mg# that would have been in Fe-Mg equilibrium with the olivine in Planetary Instrument for X-ray Lithochemistry Dourbes (Liu et al., 2022) as an example. Same projection was done for each group member in Séítah and the Mg# for the melt at equilibrium with olivines is indicated as vertical lines with color code same as the one used for targets. For Issole, the dashed line indicates values for outlier values. Black squares are from shergottites (Filiberto & Dasgupta, 2011) and black circles for chassignites (Filiberto & Dasgupta, 2011; Hewins et al., 2020).

is observed for classic examples on Earth for such cumulate sequence including the Theo's Flow in Ontario, Canada (Lentz et al., 2011; Pyke et al., 1973) and the Rum-layered series in Scotland (Emeleus et al., 1996; O'Driscoll et al., 2010). In such cumulate series, the more evolved section is in general as thick, or even thicker, than the mafic olivine-rich section. Note that a part of or the whole felsic section, might be erupted by volcanism at some stage and may not occur at the direct contact of the mafic counterpart (see discussion in Liu et al. (2022)). As discussed by Farley et al. (2022) and Wiens et al. (2022), the Máaz formation, as a whole, or part of it, could correspond to this less primitive region of the sequence. However, the careful textural, chemical, and mineralogical analysis based on SuperCam data for the Máaz formation and the uppermost Content member of the Séitah formation led Udry et al. (2022) to conclude that the succession that overlies the Séítah formation consists of a distinct family of lava flows with possible interbedded pyroclastic flows. Additionally, thermodynamic modeling also suggests that Séítah and Máaz/Content are not petrogenetically linked, and that they are likely derived from different magmatic systems (Udry et al., 2022). Such analysis supports a scenario in which the less primitive elements of the Séítah sequence would have been completely eroded before the Máaz formation and Content member was emplaced. Unfortunately, the contact between lower Máaz and Séítah below the Artuby ridge is hidden below regolith/sand dunes, which made direct observation of a potential erosional surface impossible (Figure 2). The contact between the Content member seems relatively sharp at the NE edge of the rover traverse but was not studied in detail by Perseverance. Again, no erosional surface was detected. In this scenario, given that the olivine-rich section of the cumulate series is at least 15–20 m thick (Figure 12), with the base of the section unidentified, erosion (based on the relative percentages of cumulate phases in terrestrial analogs) must have been very substantial to likely removing tens of meters of the more of pyroxene- and plagioclase-rich cumulate section. See Section 6.5 for more discussion on this topic.

6.3. Petrology of Séítah Rocks Compared to Other In Situ Olivine-Pyroxene Detections at Gale and Gusev Craters

Olivine has been found in situ in only a few of the locations explored previously robotic missions (Figure 14). At Gale crater, explored by the NASA MSL Curiosity rover, sedimentary rocks are dominant and igneous lithologies are found primarily as detrital clasts and as unaltered individual grains within sandstones. Olivine was detected

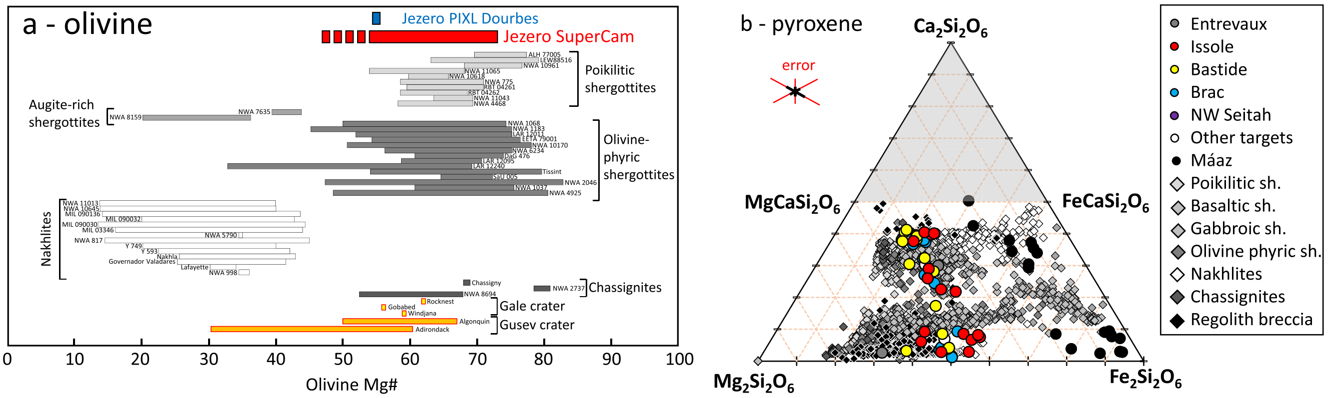

Figure 14. Composition of olivines and pyroxenes compared to Martian meteorites and other detections on Mars by previous missions. See text for references. (a) Olivine Fo# = Mg/(Fe + Mg) for olivine by SuperCam (red) and Planetary Instrument for X-ray Lithochemistry in Dourbes (blue). (b) Ternary diagram for pyroxenes. Meteorite compositions from Udry et al. (2020). Error indicated in red is the accuracy and in black is the precision for Laser-Induced Breakdown Spectroscopy, calculated at the center for ternary diagram, see text for more details.

by the CheMin instrument in the Windjana sandstone with Fo# of 59 ± 6. There, olivine is the dominant mineral together with augite with an average composition of $Wo_{37}En_{42}Fs_{21}$, Mg# = 68, and some pigeonite of average composition $Wo_{05}En_{63}Fs_{32}$, Mg# = 66 (Morrison et al., 2018; Treiman & Filiberto, 2015). The Windjana olivine has Fo# similar to that of olivine at Jezero measured by SuperCam, while the augite composition is also broadly consistent with that of Jezero augite but with slightly higher Mg#. The pigeonite composition from Windjana has a higher Mg# compared to most of Jezero pigeonite. These detrital minerals at Windjana were interpreted as possibly coming from the same basaltic igneous protolith (Treiman & Filiberto, 2015). Analogs of Séítah cumulate rocks could constitute an excellent candidate for the source protolith of these minerals, especially as such cumulate rocks concentrate these mineral phases with relatively large grain sizes. We also expect that the large grain sizes would also improve their integrity during transport and deposition. Although transport would be expected to affect the mineralogical integrity of olivine through chemical alteration and mechanical abrasion, the potential abundance of olivine derived from erosion of a cumulate source would favor the survival of at least some olivine during source-to-sink transport. CheMin also detected some olivine with Fo# 62 together with pigeonite and augite in the Rocknest soils (Bish et al., 2013), as well as trace amounts of olivine with pyroxene in the Yellowknife Bay mudstones (Vaniman et al., 2014), and in an active eolian sediment from the Namib dune at the Gobabed locality with Fo# of 56 (Achilles et al., 2017).

At Gusev crater, olivine was detected by all spectroscopic instruments, Mini-TES, Mössbauer spectroscopy and APXS, in both the Adirondack-class basaltic rocks and, in the Algonquin-class of rocks (McSween et al., 2006, 2008; Morris et al., 2006). For the Adirondack-class, olivine Fo# varies somewhat, ranging between 30 and 60 depending on the instrument. In these rocks, olivine is associated with augite, pigeonite and the dominant mineral phase plagioclase in these rocks. These rocks were interpreted as picritic basalts with modal abundances of olivine up to 20%–30% depending on the correction made for alteration phases. Although the mineralogical assemblage of these rocks bears some similarity with Séítah rocks, there are important differences, such as the larger abundance of plagioclase and the basaltic bulk composition for the Adirondack-class versus mafic to ultramafic for Séítah. The Adirondack-class basalts may have formed from primitive magmas produced by melting of undepleted mantle at depth and erupting without significant fractionation.

Algonquin-class rocks are the most similar in terms of in situ olivine-pyroxene detection to rocks of the Séítah formation. They were inferred to have high amounts of olivine, up to 30%–50%, along with pigeonite and plagioclase, and lower percentages of augite. Olivine is locally present as megacrysts, and the rocks have nearly a komatiite composition (McSween et al., 2008), similar to the bulk composition of Séítah rocks. Interestingly, the olivine within Algonquin class rocks shows a decreasing Fo# with elevation, from 67 down to 50 over ~30 m. A similar trend is observed along the traverse in Séítah (Figure 12). McSween et al. (2008) interpreted such evolution as evidence for an accumulation process of olivine during progressive fractional crystallization, which is consistent with our interpretation of Séítah rocks (Sections 6.1 and 6.2). Altogether, Séítah and Algonquin-class rocks may represent two kinds of cumulate rocks with slightly different compositions: locally Séítah, which covers a wider area, is more enriched in olivine and is less differentiated. Séítah may represent a more primitive part of the fractional crystallization system when compared to Algonquin, assuming a parental magma with similar composition. Whatever the emplacement mechanism, as either an extrusive lava flow/pond, an intrusive sill, a small laccolith, an impact melt sheet, or ejecta melt pond, these occurrences suggest that such rocks may not be rare at the surface of Mars.

6.4. Petrology of Séítah Rocks Compared With Martian Meteorites

Comparison with Martian meteorites is instructive as well (Figure 14). In the TAS $Na_2O + K_2O$ versus SiO_2 diagram, the Séítah rocks fall in the same field as most shergottites, have higher SiO_2 and alkali contents compared to chassignites, and lower SiO_2 compared to nakhlites (Figure S5 in Supporting Information S1). In other geochemical diagrams, rocks from Brac, Bastide, and NW Séítah are, as a whole, very rich in MgO, rich in FeOT, and contain moderate CaO and relatively low Al_2O_3. This makes their composition, and mineral assemblage, most similar to shergottites *sensus lato* (Papike et al., 2009; Udry et al., 2020), and more specifically to olivine-phyric and poikilitic shergottites (Combs et al., 2019; Rahib et al., 2019), although these compositions are also fairly close to the richest MgO chassignites (Hewins et al., 2020). Rocks from the Issole region are slightly different as they contain less MgO and more Al_2O_3, making their composition still comparable to shergottites but more to the basaltic endmember of shergottites. Note that the average of all Séítah rocks has lower CaO compared to nakhlites. Except for the Issole group, they are richer in MgO than the various igneous clasts of the regolith breccia Northwest Africa (NWA) 7034/7533 and paired samples (e.g., Hewins et al., 2017; Santos et al., 2015), including the least differentiated ones.

Olivine is a common mineral in most Martian meteorites, together with pyroxene (Figure 14). In the laboratory, olivine is typically analyzed by electron microprobe and/or scanning electron microscopy at high spatial resolution, making possible the study of internal chemical zoning which is common in the Martian meteorites. It is not possible to replicate this type of analysis with SuperCam LIBS, although the shot-to-shot data represent an in-depth chemical profile over tens of μm within grains. Within the shot-to-shot data of olivine phases in Séitah, we did not observe any significant trend in Mg# during the laser burst, which suggests that Séítah olivine grains do not have marked chemical zoning. This is consistent with many olivine cumulate samples, including poikilitic shergottites and chassignites (McCubbin et al., 2013; Udry & Day, 2018), that underwent cooling rates that allowed for Fe-Mg equilibration, which occurs relatively rapidly (e.g., Gaetani & Watson, 2002 and references therein). In addition, PIXL maps of the Dourbes abraded patch show no clear zonation in the olivine grains at a 120 μm scale nor between different olivine grains in Brac. Séítah olivine Fo#s fall in the same range as the Fo#s of poikilitic and olivine-phyric shergottites as well as chassignites but are consistently higher than olivine Fo#s in nakhlites (Figure 14a).

Augite pyroxenes in Séítah also have compositions that are consistent with many martian meteorites. Augite grains with Wo# > 35 have similar compositions to some pyroxenes from chassignites, for example, NWA 8694, some clasts in the regolith breccia NWA 7034/NWA 7533 and paired samples (Hewins et al., 2017; Santos et al., 2015; Wittmann et al., 2015), and some olivine-phyric shergottites, but also with the highest Mg# augite (core) in nakhlites (McCubbin et al., 2013; Treiman, 2005; Udry & Day, 2018). Augites with Wo < 35 have similar compositions to pyroxene in gabbroic shergottites, olivine-phyric shergottites and some igneous clasts of the regolith breccia NWA 7034/NWA 7533 (Hewins et al., 2017; Papike et al., 2009; Santos et al., 2015; Udry et al., 2020; Wittmann et al., 2015). In the augites with Wo < 35, Mg# is slightly lower than equivalent pyroxene in chassignites and in most poikilitic shergottites. The case of pigeonite and orthopyroxene is different and somewhat striking. A few grains have compositions and high Mg#s comparable to the pigeonite composition in olivine-phyric and poikilitic shergottites as well as to the chassignite NWA 8694. However, most pigeonite and othopyroxene grains are more ferroan with compositions similar to low-Ca pyroxenes from nakhlites (McCubbin et al., 2013), or from some pyroxenes contained in microbasaltic clasts in the regolith breccia NWA 7034/NWA 7533 and paired samples (Hewins et al., 2017; Santos et al., 2015; Wittmann et al., 2015).

Like some shergottites and chassignites, Séítah rocks are cumulate rocks, indicating that density-driven fractionation processes are not rare on Mars. Analysis of textures from the micro-context imager RMI taken under different color lights and XRF maps by the PIXL instrument of the Dourbes abraded patch show clear poikilitic texture with augite crystals mantling olivine crystals (Liu et al., 2022). In terms of bulk and mineralogical composition, Liu et al. (2022) noticed some similarities with poikilitic shergottites and chassignite NWA 8694, but also some differences like the absence of pigeonite in PIXL data, and possibly differences in accessory minerals like phosphate mineralogy. SuperCam LIBS has detected pigeonite in various rocks, but the composition of this pigeonite is generally different overall, for example, more ferroan, compared with pigeonite in shergottites and chassignites. Altogether, the Séítah rocks show the strongest similarities in terms of bulk chemistry and mineralogical composition with poikilitic shergottites, and also with chassignite NWA 8694.

6.5. Structure and Exhumation of Séítah

Séítah is the stratigraphically lowest and could be the oldest formation of the Jezero crater floor. Based on geomorphic expression and mineralogy from orbital data, Goudge et al. (2015) mapped Séítah and its inferred equivalents (their "light-toned floor unit") as being exposed primarily to the outer edge of the crater floor while the central region is dominantly covered by the Máaz formation (their "volcanic floor unit"). Higher-resolution mapping (Holm-Alwmark et al., 2021; Stack et al., 2020) demonstrates that exposures of this formation in the region where Perseverance landed represent depositional or erosional inliers into the Máaz formation. Remarkably, in most areas, Séítah is generally topographically higher than the surrounding Máaz formation although it is stratigraphically older. A key characteristic of the Séítah formation is that it shows evidence of stratification that is nearly horizontal over large areas imaged by Perseverance. Along the rover traverse, the portion of Séítah that can be observed above ground by imaging (J. F. Bell et al., 2022; this study), and below ground by RIMFAX (Hamran et al., 2022) indicates that Séítah gently dips and plunges below Máaz close to the contact with this formation. Orbital data do not permit detailed characterization of Séítah stratification, but the fact that no obvious large-scale stratification is observed in Séítah from orbit is consistent with horizontal stratification. On a broad scale, having Séítah rocks distributed topographically higher than Máaz could be a consequence of the crater structure at depth with material more exhumed on the outer edge of the crater floor (Séítah) compared to the central region (Máaz).

On a local scale, in the area visited by Perseverance, Séítah is exposed in an inlier, a window into stratigraphically deeper, older material below Máaz (Wiens et al., 2022). As shown in Figure 12 and by Wiens et al. (2022), the structure of Séítah forms a long-wavelength: "fold" along the rover traverse that might be extrapolated to a long-wavelength, flat, dome for this area of Séítah. In terms of structure, a dome actually implies differential vertical movement between the center and the edges of the formation. This implies more exhumation of deeper rocks now exposed near the center of the dome. Noticeably, the Máaz formation is also locally affected by the doming as attested by the beds tilting to the southwest at Artuby ridge, which means that such doming would have occurred after the emplacement of Máaz assuming it was originally horizontal. Of course, erosion has certainly played a key role, and was likely not uniform with more erosion affecting the center than the edges of the Séítah inlier. To be activated and efficient, erosion requires a differential vertical movement, here a local differential uplift of Séítah with respect to Máaz to exhume Séítah from below Máaz. On Earth, such dome structure can be anticlines due to tectonic stresses triggering fold formation generally observed in sedimentary rocks. On Mars, plate tectonics is absent, and there is no mechanism known to trigger large horizontal movements and the formation of folds. Another possible process is local diapirism that can also generate dome structures by injecting less dense material into denser surrounding rocks. It is unlikely here as the Séítah formation appears composed of ultramafic minerals and is therefore composed by the densest rocks found in the Jezero crater floor (Wiens et al., 2022). Diapiric uplift could potentially happen in case of local strong alteration and hydration of ultramafic lithology that generate serpentine and other alteration products, which would decrease the overall density of Séítah rocks. However, our observations show that the Séítah rocks are little altered, and the density of such rocks is higher than that of the overlying Máaz formation (Wiens et al., 2022), making this hypothesis unlikely.

Another possibility is the local injection and underplating of material, likely magma, below the highest areas of Séítah. Such a magma underplating process can generate doming in the above formation not only to account for the excess material injected at depth, but also by the thermal stress it generates in the overlying formations. Such thermal uplift has been described on Earth in various contexts, for instance at the base of the continental lithosphere (e.g., Thybo & Artemieva, 2013 and references therein) or in the old Ordovician lithosphere prior to the Pyrenean orogeny in France and Spain (Puddu et al., 2019). In such a process, magma injection and underplating generate thermal thinning and stretching of the overlying lithosphere, with a subsequent increase of the geothermal gradient and possible metamorphic overprinting. Such a metamorphic event is not observed for Séítah and for the adjacent Máaz rocks, either because it did not occur, or because it is not well expressed in the mineralogical assemblage of the rocks. Future thermomechanical modeling and analysis of returned samples will help test these hypotheses as well as the impact melt scenario for the structure of the formation.

Another point regards the timing for the exhumation of Séítah with respect to the lacustrine activity/period in Jezero crater. Overall, even with some minor hydrated phases and carbonates detected in Séítah, these rocks appear relatively pristine with weak to intermediate evidence of alteration. The highest amounts of alteration occur in the portions of the Séítah formation that are closest to the overlying Máaz formation (i.e., in the Issole region). Olivine is generally prone to alteration in the presence of water and readily generates a variety of secondary phases such as various kinds of smectites, serpentines, brucite and/or magnetite. Of course, this alteration depends on various environmental parameters (e.g., temperature, water activity, pH, duration), and on the olivine composition and mineral assemblage (Lamadrid et al., 2017; Montserrat et al., 2017 and references therein). In addition, in the presence of CO_2 for instance, olivine-rich rocks may be carbonated resulting in various carbonate phases depending as well on environmental conditions and/or rock composition (Kelemen et al., 2021; Montserrat et al., 2017; Ulven et al., 2017). If the Séítah rocks encountered by Perseverance had been exposed for a long period to water in a lake, such alteration processes could have occurred. This does not appear to be the case, at least not massively, suggesting that the area of Séítah visited by Perseverance was not yet exhumed at the surface at the period of the lake activity, or that the lake activity was short (Wiens et al., 2022). However, we cannot rule out the possibility that part of shallow Séítah was altered and then completely eroded. The Máaz formation, which is locally more altered (Mandon et al., 2022), does not contain olivine and is dominated by pyroxene and plagioclase (Udry et al., 2022), two minerals that are generally more resistant than olivine to aqueous alteration at surface conditions. Therefore, a possible scenario would be that Máaz was more extensive at the time of the lake activity and protected the Séítah formation below (or at least the area visited by Perseverance), which was exhumed later, when the lake had already retreated.

Séítah is part of the regional Nili Fossae olivine-carbonate unit. Discovering igneous, olivine-rich (up to 60%) cumulate rocks in Séítah was surprising. From orbital observations, the nature of the regional olivine-carbonate unit has actually been discussed as possible lava flows (Tornabene et al., 2008), impact product of Isidis (Mustard et al., 2007; Palumbo & Head, 2018), pyroclastic deposits (Bramble et al., 2017; Kremer et al., 2019; Mandon et al., 2020; Rogers et al., 2018), or sedimentary deposits (Rogers et al., 2018; Stack et al., 2020). None of these hypotheses is fully consistent with the cumulate nature of Séítah described by Perseverance. That may suggest that this regional unit is rather composed by distinct sub-units, some igneous, some sedimentary, with various origins. Future investigations by Perseverance on the crater rims and outside of Jezero elsewhere in the olivine-carbonate unit will be important to determine this possible diversity and possible emplacement scenarios.

6.6. Séítah Samples for Mars Sample Return: Some Possible Future Investigations

Two pairs of samples have been collected in Séítah: the Salette and Coulette cores at the Brac outcrop, and the Robine and Malay cores at the Issole outcrop. One of each pair has been deposited in the contingency cache at the base of the delta, and the second will be deposited in the final cache later in the mission (Simon et al., 2023; Sun et al., 2023). These samples would obviously be critical to tackle some of the scientific questions discussed in this article using the higher spatial resolution and analytical precision of laboratory instruments on Earth. For igneous petrology, careful microtextural analyses down to the sub-μm scale would strengthen the chemical and mineralogical analyses done on Mars, including the study of possible subtle chemical zoning of major and/or trace elements. For instance, the pigeonite and orthopyroxene detected by SuperCam LIBS but not observed by PIXL, and which seems in disequilibrium with olivine and augite, should be further studied microtexturally and chemically. This will be important to determine precisely when, why and how it crystallized during the magmatic evolution.

Mineral and/or fluid inclusions should be investigated as well as possible mineral exsolutions in olivine and pyroxenes. Volatiles, H_2O but also C-bearing species such as CO_2 or CH_4, should be studied by a combination of spectroscopic and SIMS techniques to identify these volatiles and quantify their abundances and isotopic compositions in the Séítah magma. The origin, abundance, and isotopic composition of water in the Martian mantle, and its consequences for the physicochemical evolution of Mars are still a matter of debate (Barnes et al., 2020; Breuer et al., 2016; Dong et al., 2022; Filiberto et al., 2016). Water could be present not only in phosphates or in the mesostasis in Séítah rocks but also in trace abundances in nominally anhydrous minerals (D. R. Bell & Rossman, 1992) such as olivine (Bolfan-Casanova et al., 2014) and pyroxene (Peslier et al., 2002). Stable isotopes, measured for the bulk rock and in situ for each mineral phase, could also be critical to better define the source for the Séítah rocks. Importantly, studying in detail primary melt inclusions in olivines and/or the pattern of trace elements, for example, REE (Basu Sarbadhikari et al., 2009, 2011), could help constrain the parental magma for Séítah and its volatile content, and possible differences between Brac and Quartier. The possible petrogenetic link between Séítah and Máaz could also be clearly established through an examination of returned samples. Fe-Ti-Cr oxides also require laboratory analytical facilities to precisely determine their chemistry and Fe valency, with important implications for the knowledge of redox processes during magmatic and alteration processes in these rocks.

Séítah may be the oldest formation exposed on the crater floor of Jezero, and any geochronological constraints would be important in clarifying the igneous evolution of Jezero and of Mars in general. Phosphates are present in these rocks (Liu et al., 2022; this study) and baddeleyites, even if not observed by rover instruments, are likely present in these rocks; they are also detected in many analog Martian meteorites. Crystallization and cooling ages could be obtained to understand the timing of formation, and then the temporal evolution of these rocks. Low-temperature thermochronometers could also be used to constrain the final exhumation of Séítah, in particular its timing of emplacement with respect to the deltaic-lacustrine strata in the crater (see previous sections). Hence, these data could be important to constrain the lake activity and its timing in this region of Mars. Séítah is likely not the best formation for crater retention compared to the Máaz formation, for instance. That can be due to the lithology itself, erosion, the timing of exhumation to the surface, or a combination of all these. In any case, geochronological data for Séítah should help to constrain the relationship between Máaz and Séítah. For example, an extended time interval between them would mean that the contact may indeed be an erosional surface, as discussed in previous sections.

As the oldest formation, Séítah could also provide important constraints for the magnetic field of Mars. Fe-oxides are present, some being likely primary, and could carry a magnetic signal important to constrain the magnitude and evolution with time of the Martian magnetic field.

Laboratory investigations should also be critical to better constrain the alteration of Séítah rocks: it is subtle, yet it is present (see Tice et al. (2022), Clavé et al. (2022) and Mandon et al. (2022)). If the protolith is proven to be the same in terms of chemistry, Issole being likely more altered than Brac, these rocks will offer a unique opportunity to characterize a gradient of alteration and associated chemical mass transfers. Techniques at high spatial resolution, for example, transmission electron microscopy, XANES spectroscopy, will be used to characterize fine alteration phases such as serpentines and other silicates, Fe-oxides, or brucite, which are generally nano-textured. Carbonates or sulfates would be sought out, their chemistry would be analyzed as well as their degree of hydration/hydroxylation by vibrational spectroscopies (Raman, IR). Olivine in Séítah appears relatively pristine at the spatial resolution of PIXL and SuperCam LIBS, but they could be altered superficially, triggering the formation of passivation layers that may protect the olivine grains from further alteration (Daval et al., 2011). Altered ultramafics, even at the onset of alteration, may form a favorable niche for hosting life. Any putative organic carbon could be tracked in the laboratory and if some organics are found, their chemistry, isotopic composition and structure will be completely characterized to discuss their possible biogenicity (see possible strategies in Bernard and Papineau (2014)).

7. Conclusion

The Perseverance rover discovered surprising rocks in the deepest formation of the Jezero crater floor called Séítah. Geochemical and mineralogical data collected by the SuperCam instrument over large exposures of Séítah confirm the preliminary description by Liu et al. (2022) and Wiens et al. (2022): the Séítah formation consists of igneous cumulate rocks dominated by millimetric grains of olivine with the presence of augite and pigeonite pyroxenes, and other minor primary mineral phases (e.g., plagioclase, Cr-Fe-Ti oxides, phosphates). SuperCam data display some chemical and mineralogical variability along a 140 m long traverse, corresponding to ∼15–20 m thickness, in southeastern Séítah. Séítah rocks closest to the boundary with the overlying Máaz formation have a lower grain size together with lower bulk rock Mg# , lower olivine content and they are generally enriched in Al_2O_3. These rocks also show more alteration phases such as carbonate, sulfate, perchlorate, and clays. Going deeper in the formation, rock Mg#, olivine content and grain size increase and the rocks are globally weakly altered. These findings rule out a sedimentary origin for Séitah and confirm that the two major formations of the Jezero crater floor, Séítah (this study) and Máaz (Udry et al., 2022), are igneous.

These observations are consistent with the chemical and mineralogical stratification expected in the mafic to ultra-mafic part of a cumulate series with denser liquidus phases (olivine) at the bottom and more differentiated composition at shallower levels. Some investigations in the Northwest part of Séítah closer to the Jezero delta as well as numerous long-distance RMI-VISIR data covering large exposures of inner Séítah show similar features, suggesting that this conclusion may apply to the whole formation, at least in the area visited by Perseverance. The Máaz formation may represent the felsic (pyroxene- and plagioclase-rich) part of the cumulate series (Farley et al., 2022; Wiens et al., 2022). However, the contrasted chemistry of rocks and pyroxenes as well as thermodynamic modeling suggest that Máaz and Séítah are likely not petrogenetically linked, and that they may come from different magmas and/or sources. Future in situ data in the olivine-carbonate unit and further modeling will help test this hypothesis.

The Séítah rocks show textural, geochemical, and mineralogical similarities with the Algonquin rocks at Gusev crater (McSween et al., 2008), and with Martian meteorites such as poikilitic shergottites and chassignites. This suggests that such olivine cumulate rocks may not be rare at the surface of Mars and raises important questions on the magmatic processes at work for their formation. Because such rocks are expected to crystallize slowly at depth, their presence on the crater floor also opens questions on the exhumation and erosion processes in Jezero crater. The two samples collected at Issole and Brac should provide important constraints when they would be returned to Earth and analyzed in the laboratory to answer these questions.

Perseverance is now exploring the Jezero delta after the crater floor formations (Sun et al., 2023). Then, the rover should explore the marginal units and, ultimately, should leave Jezero crater for an extended mission in the NE Syrtis region if things go well. All along this traverse, Perseverance should encounter various sections of the regional olivine-carbonate unit mapped from orbit. In situ exploration by Perseverance will establish whether the olivine cumulate like Séítah is observed elsewhere in this unit, which would indicate Séítah is part of a very extended and thick cumulate unit, much bigger than most examples known on Earth. Alternatively, this unit may not be a single unit as olivine and carbonate may be present in various deposits not easily distinguished from orbit, such as olivine-rich basaltic flows, pyroclastic flows, sedimentary rocks, or other types of cumulate rocks.

Data Availability Statement

The data in this publication are from the SuperCam, MastCam-Z, and WATSON instruments, and the NavCam cameras of the Mars 2020 Perseverance rover. The SuperCam data include the Laser Induced Breakdown Spectroscopy (LIBS), Visible/near infrared (VISIR) Spectroscopy, and the Remote Micro-Imager (RMI). The SuperCam major element oxide composition (MOC), total emissivity, and all raw data and processed calibrated data files are included in the Planetary Data System (Wiens & Maurice, 2021). The MastCam-Z, WATSON, and NavCam data sets are also included in the Planetary Data System by J. F. Bell and Maki (2021), Beegle (2021), and Maki (2020), respectively. In addition, all image data presented here from the SuperCam and Mastcam-Z instruments are available through the Planetary Data System Imaging Node (https://pds-imaging.jpl.nasa.gov/portal/mars2020_mission.html) and GeoSciences Node (https://pds-geosciences.wustl.edu/missions/mars2020/).

Acknowledgments
This paper benefited from comments by two anonymous reviewers as well as from thorough reading by editor Laurent Montesi and the associate editor. The authors grateful acknowledge the Mars2020 and SuperCam Science and Engineering teams. Funding by NASA Mars exploration program, CNES and LANL is acknowledged. YL's research was carried out at the Jet Propulsion Laboratory, California Institute of Technology, under a contract with the National Aeronautics and Space Administration (80NM0018D0004). The decision to implement Mars Sample Return will not be finalized until NASA's completion of the National Environmental Policy Act (NEPA) process. This document, including its descriptions of planned Earth-based analyses of the Mars samples being collected by the Perseverance rover, is being made available for information purposes only.

References

Achilles, C. N., Downs, R. T., Ming, D. W., Rampe, E. B., Morris, R. V., Treiman, A. H., et al. (2017). Mineralogy of an active eolian sediment from the Namib dune, Gale crater, Mars. *Journal of Geophysical Research: Planets*, *122*(11), 2344–2361. https://doi.org/10.1002/2017JE005262

Adams, J. B. (1974). Visible and near IR diffuse reflectance spectra of pyroxenes as applied to remote sensing of solid objects in the solar system. *Journal of Geophysical Research*, *79*(32), 4829–4836. https://doi.org/10.1029/JB079i032p04829

Allwood, A. C., Wade, L. A., Foote, M. C., Elam, W. T., Hurowitz, J. A., Battel, S., et al. (2020). PIXL: Planetary instrument for X-ray Lithochemistry. *Space Science Reviews*, *216*(8), 134. https://doi.org/10.1007/s11214-020-00767-7

Anderson, R. B., Forni, O., Cousin, A., Wiens, R. C., Clegg, S. M., Frydenvang, J., et al. (2022). Post-landing major element quantification using SuperCam laser induced breakdown spectroscopy. *Spectrochimica Acta Part B: Atomic Spectroscopy*, *188*, 106347. https://doi.org/10.1016/j.sab.2021.106347

Anderson, R. B., Gabriel, T. S., Forni, O., Manrique, J. A., Gasda, P., Vogt, D., & Ollila, A. M. (2023). Trace and minor element quantification with SuperCam laser induced Breakdown spectroscopy (LIBS). In *54th Lunar and Planetary Science Conference 2023* (p. 2182). Retrieved from https://www.hou.usra.edu/meetings/lpsc2023/pdf/2182.pdf

Alwmark, S., Horgan, B., Udry, A., Bechtold, A., Fagents, S., Ravanis, E., et al. (2023). Diverse lava flow morphologies in the stratigraphy of the Jezero crater floor. *Journal of Geophysical Research: Planets*, e2022JE007446. https://doi.org/10.1029/2022JE007446

Barnes, J. J., McCubbin, F. M., Santos, A. R., Day, J. M. D., Boyce, J. W., Schwenzer, S. P., et al. (2020). Multiple early-formed water reservoirs in the interior of Mars. *Nature Geoscience*, *13*(4), 260–264. https://doi.org/10.1038/s41561-020-0552-y

Basu Sarbadhikari, A., Day, J. M. D., Liu, Y., Rumble, D. III, & Taylor, L. A. (2009). Petrogenesis of olivine-phyric shergottite Larkman Nunatak 06319: Implications for enriched components in martian basalts. *Geochimica et Cosmochimica Acta*, *73*(7), 2190–2214. https://doi.org/10.1016/j.gca.2009.01.012

Basu Sarbadhikari, A., Goodrich, C. A., Liu, Y., Day, J. M. D., & Taylor, L. A. (2011). Evidence for heterogeneous enriched shergottite mantle sources in Mars from olivine-hosted melt inclusions in Larkman Nunatak 06319. *Geochimica et Cosmochimica Acta*, *75*(22), 6803–6820. https://doi.org/10.1016/j.gca.2011.09.001

Beegle, L. (2021). Mars 2020 SHERLOC bundle [Dataset]. NASA Planetary Data System. https://doi.org/10.17189/1522643

Bell, D. R., & Rossman, G. R. (1992). Water in Earth's mantle: The role of nominally anhydrous minerals. *Science*, *255*(5050), 1391–1397. https://doi.org/10.1126/science.255.5050.1391

Bell, J. F., & Maki, J. N. (2021). Mars 2020 Mast camera zoom bundle [Dataset]. NASA Planetary Data System. https://doi.org/10.17189/1522843

Bell, J. F., Maki, J. N., Alwmark, S., Ehlmann, B. L., Fagents, S. A., Grotzinger, J. P., et al. (2022). Geological and meteorological imaging results from the Mars 2020 Perseverance rover in Jezero crater. *Science Advances*, *8*, abo4856. https://doi.org/10.1126/sciadv.abo4856

Bell, J. F., Maki, J. N., Mehall, G. L., Ravine, M. A., Caplinger, M. A., Bailey, Z. J., et al. (2021). The Mars 2020 perseverance rover Mast camera zoom (Mastcam-Z) multispectral, stereoscopic imaging investigation. *Space Science Reviews*, *217*(1), 24. https://doi.org/10.1007/s11214-020-00755-x

Bernard, S., & Papineau, D. (2014). Graphitic carbons and biosignatures. *Elements*, *10*(6), 345–350. https://doi.org/10.2113/gselements.10.6.435

Beyssac, O. (2020). New trends in Raman spectroscopy: From high-resolution geochemistry to planetary exploration. *Elements*, *16*(2), 117–122. https://doi.org/10.2138/gselements.16.2.117

Bhartia, R., Beegle, L. W., DeFlores, L., Abbey, W., Razzell Hollis, J., Uckert, K., et al. (2021). Perseverance's scanning habitable environments with Raman and luminescence for organics and chemicals (SHERLOC) investigation. *Space Science Reviews*, *217*(4), 58. https://doi.org/10.1007/s11214-021-00812-z

Bish, D. L., Blake, D. F., Vaniman, D. T., Chipera, S. J., Morris, R. V., Ming, D. W., et al. (2013). X-Ray diffraction results from Mars Science Laboratory: Mineralogy of rocknest at Gale crater. *Science*, *341*(6153), 1238932. https://doi.org/10.1126/science.1238932

Blake, D. F., Morris, R. V., Kocurek, G., Morrison, S. M., Downs, R. T., Bish, D., et al. (2013). Curiosity at Gale crater, Mars: Characterization and Analysis of the Rocknest sand shadow. *Science*, *341*(6153). https://doi.org/10.1126/science.1239505

Bolfan-Casanova, N., Montagnac, G., & Reynard, B. (2014). Measurement of water contents in olivine using Raman spectroscopy. *American Mineralogist*, *99*, 149–156. https://doi.org/10.2138/am.2014.4444

Bramble, M. S., Mustard, J. F., & Salvatore, M. R. (2017). The geological history of northeast Syrtis major, Mars. *Icarus*, *293*, 66–93. https://doi.org/10.1016/j.icarus.2017.03.030

Breuer, D., Plesa, A., Tosi, N., & Grott, M. (2016). Water in the Martian interior—The geodynamical perspective. *Meteoritics & Planetary Sciences*, *51*(11), 1959–1992. https://doi.org/10.1111/maps.12727

Brown, A. J., Viviano, C. E., & Goudge, T. A. (2020). Olivine-carbonate mineralogy of the Jezero crater region. *Journal of Geophysical Research: Planets*, *125*(3), e2019JE006011. https://doi.org/10.1029/2019JE006011

Chide, B., Maurice, S., Cousin, A., Bousquet, B., Mimoun, D., Beyssac, O., et al. (2020). Recording laser-induced sparks on Mars with the SuperCam microphone. *Spectrochimicia Acta B*, *174*, 106000. https://doi.org/10.1016/j.sab.2020.106000

Chide, B., Maurice, S., Murdoch, N., Lasue, J., Bousquet, B., Jacob, X., et al. (2019). Listening to laser sparks: A link between laser-induced breakdown spectroscopy, acoustic measurements and crater morphology. *Spectrochimica Acta Part B: Atomic Spectroscopy*, *153*, 50–60. https://doi.org/10.1016/j.sab.2019.01.008

Clavé, E., Benzerara, K., Meslin, P. Y., Forni, O., Royer, C., Mandon, L., et al. (2022). Carbonate detection with SuperCam in igneous rocks on the floor of Jezero Crater, Mars. *Journal of Geophysical Research: Planets*, e2022JE007463. https://doi.org/10.1029/2022JE007463

Clegg, S. M., Wiens, R. C., Anderson, R., Forni, O., Frydenvang, J., Lasue, J., et al. (2017). Recalibration of the Mars Science Laboratory ChemCam instrument with an expanded geochemical database. *Spectrochimica Acta Part B: Atomic Spectroscopy*, *129*, 64–85. https://doi.org/10.1016/j.sab.2016.12.003

Cloutis, E. A., & Gaffey, M. J. (1991). Spectral-compositional variations in the constituent minerals of mafic and ultramafic assemblages and remote sensing implications. *Earth, Moon, and Planets*, *53*(1), 11–53. https://doi.org/10.1007/BF00116217

Combs, L. M., Udry, A., Howarth, G. H., Righter, M., Lapen, T. J., Gross, J., et al. (2019). Petrology of the enriched poikilitic shergottite Northwest Africa 10169: Insight into the martian interior. *Geochimica et Cosmochimica Acta*, *266*, 435–462. https://doi.org/10.1016/j.gca.2019.07.001

Cousin, A., Dehouck, E., Meslin, P.-Y., Forni, O., Williams, A. J., Stein, N., et al. (2017). Geochemistry of the Bagnold dune field as observed by ChemCam and comparison with other aeolian deposits at Gale Crater. *Journal of Geophysical Research: Planets*, *122*(10), 2144–2162. https://doi.org/10.1002/2017JE005261

Cousin, A., Sautter, V., Fabre, C., Dromart, G., Montagnac, G., Drouet, C., et al. (2022). SuperCam calibration targets on board the perseverance rover: Fabrication and quantitative characterization. *Spectrochimica Acta Part B: Atomic Spectroscopy*, *188*, 106341. https://doi.org/10.1016/j.sab.2021.106341

Cremers, D. A., & Radziemski, L. J. (2013). *Handbook of laser-induced Breakdown spectroscopy, elemental analysis* (2nd ed.). Wiley Online Library. https://doi.org/10.1002/9781118567371

Daval, D., Sissmann, O., Menguy, N., Saldi, G. D., Guyot, F., Martinez, I., et al. (2011). Influence of amorphous silica layer formation on the dissolution rate of olivine at 90°C and elevated pCO_2. *Chemical Geology*, *284*(1–2), 193–209. https://doi.org/10.1016/j.chemgeo.2011.02.021

Dong, J., Fischer, R. A., Stixrude, L. P., Lithgow-Bertelloni, C. R., Eriksen, Z. T., & Brennan, M. C. (2022). Water storage capacity of the martian mantle through time. *Icarus*, *385*, 115113. https://doi.org/10.1016/j.icarus.2022.115113

Edwards, C. S., & Ehlmann, B. L. (2015). Carbon sequestration on Mars. *Geology*, *43*(10), 863–866. https://doi.org/10.1130/G36983.1

Ehlmann, B. L., Edgett, K. S., Sutter, B., Achilles, C. N., Litvak, M. L., Lapotre, M. G. A., et al. (2017). Chemistry, mineralogy, and grain properties at Namib and High dunes, Bagnold dune field, Gale crater, Mars: A synthesis of curiosity rover observations. *Journal of Geophysical Research: Planets*, *122*, 2510–2543. https://doi.org/10.1002/2017JE005267

Emeleus, C. H., Cheadle, M. J., Hunter, R. H., Upton, B. G. J., & Wadsworth, W. J. (1996). The Rum layered suite. In R. G. Cawthorn (Ed.), *Developments in petrology* (Vol. 15, pp. 403–439). Elsevier. https://doi.org/10.1016/S0167-2894(96)80014-5

Farley, K. A., Stack Morgan, K. M., Shuster, D. L., Horgan, B. H. N., Tarnas, J. D., Simon, J. I., et al. (2022). Aqueously altered igneous rocks on the floor of Jezero crater, Mars. *Science*, *377*(6614), eabo2196. https://doi.org/10.1126/science.abo2196

Farley, K. A., Williford, K. H., Stack, K. M., Bhartia, R., Chen, A., de la Torre, M., et al. (2020). Mars 2020 mission overview. *Space Science Reviews*, *216*(8), 142. https://doi.org/10.1007/s11214-020-00762-y

Farley, K. A., Williford, K. H., Stack, K. M., Bhartia, R., Chen, A., de la Torre, M., et al. (2021). Mars 2020 mission overview. *Space Science Reviews*, *216*(8), 142. https://doi.org/10.1007/s11214-020-00762-y

Fassett, C. I., & Head, J. W. (2005). Fluvial sedimentary deposits on Mars: Ancient deltas in a crater lake in the Nili Fossae region. *Geophysical Research Letters*, *32*(14), 2137. https://doi.org/10.1029/2005GL023456

Fau, A., Beyssac, O., Gauthier, M., Cousin, A., Meslin, P. Y., Benzerara, K., et al. (2019). Pulsed laser-induced heating of mineral phases: Implications for laser-induced breakdown spectroscopy combined with Raman spectroscopy. *Spectrochimica Acta Part B: Atomic Spectroscopy*, *160*, 105687. https://doi.org/10.1016/j.sab.2019.105687

Filiberto, J., Baratoux, D., Beaty, D., Breuer, D., Farcy, B. J., Grott, M., et al. (2016). A review of volatiles in the Martian interior. *Meteoritics & Planetary Sciences*, *51*(11), 1935–1958. https://doi.org/10.1111/maps.12680

Filiberto, J., & Dasgupta, R. (2011). Fe^{2+}-Mg partitioning between olivine and basaltic melts: Applications to Genesis of olivine-phyric shergottites and conditions of melting in the martian interior. *Earth and Planetary Science Letters*, *304*(3–4), 527–537. https://doi.org/10.1016/j.epsl.2011.02.029

Forni, O., Beck, P., Johnson, J. R., Dehouck, E., Quantin-Nataf, C., Beyssac, O., et al. (2023). Combining SuperCam LIBS and VISIR: Constraining the mineralogy in Jezero crater. In *54th Lunar and Planetary Science Conference 2023* (Vol. 2023, p. 1244). Retrieved from https://www.hou.usra.edu/meetings/lpsc2023/pdf/1244.pdf

Forni, O., Gaft, M., Toplis, M. J., Clegg, S. M., Maurice, S., Wiens, R. C., et al. (2015). First detection of fluorine on Mars: Implications for Gale crater's geochemistry. *Geophysical Research Letters*, *42*, 1020–1028. https://doi.org/10.1002/2014GL062742

Fouchet, T., Reess, J.-M., Montmessin, F., Hassen-Khodja, R., Nguyen-Tuong, N., Humeau, O., et al. (2022). The SuperCam infrared spectrometer for the perseverance rover of the Mars2020 mission. *Icarus*, *373*, 114773. https://doi.org/10.1016/j.icarus.2021.114773

Gaetani, G. A., & Watson, E. B. (2002). Modeling the major-element evolution of olivine-hosted melt inclusions. *Chemical Geology*, *183*(1–4), 25–41. https://doi.org/10.1016/S0009-2541(01)00370-9

Gasda, P. J., Anderson, R. B., Cousin, A., Forni, O., Clegg, S. M., Ollila, A., et al. (2021). Quantification of manganese for ChemCam Mars and laboratory spectra using a multivariate model. *Spectrochimica Acta Part B: Atomic Spectroscopy*, *181*, 106223. https://doi.org/10.1016/j.sab.2021.106223

Goudge, T. A., Mustard, J. F., Head, J. W., Fassett, C. I., & Wiseman, S. M. (2015). Assessing the mineralogy of the watershed and fan deposits of the Jezero crater paleolake system, Mars. *Journal of Geophysical Research: Planets*, *120*(4), 1689–1808. https://doi.org/10.1002/2014JE004782

Hamilton, V. E., & Christensen, P. R. (2005). Evidence for extensive olivine-rich bedrock in Nili Fossae, Mars. *Geology*, *33*(6), 433–436. https://doi.org/10.1130/g21258.1

Hamran, S.-E., Paige, D. A., Allwood, A., Amundsen, H. E. F., Berger, T., Brovoll, S., et al. (2022). Ground penetrating radar observations of subsurface structures in the floor of Jezero crater, Mars. *Science Advances*, *8*(34), eabp8564. https://doi.org/10.1126/sciadv.abp8564

Hewins, R. H., Humayun, M., Barrat, J. A., Zanda, B., Lorand, J. P., Pont, S., et al. (2020). Northwest Africa 8694, a ferroan chassignite: Bridging the gap between nakhlites and chassignites. *Geochimica et Cosmochimica Acta*, *282*, 201–226. https://doi.org/10.1016/j.gca.2020.05.021

Hewins, R. H., Zanda, B., Nemchin, A., Lorand, J. P., Pont, S., Pont, S., et al. (2017). Regolith breccia Northwest Africa 7533: Mineralogy and petrology with implications for early Mars. *Meteoritics & Planetary Sciences*, *52*(1), 89–124. https://doi.org/10.1111/maps.12740

Hoefen, T. M., Clark, R. N., Banfield, J. L., Smith, M. D., Pearl, J. C., & Christensen, P. R. (2003). Discovery of olivine in the Nili Fossae region of Mars. *Science*, *302*(5645), 627–630. https://doi.org/10.1126/science.1089647

Hollocher, K. (2004). *CIPW Norm calculation program*. Geology Department.

Holm-Alwmark, S., Kinch, K. M., Hansen, M. D., Shahrzad, S., Svennevig, K., Abbey, W. J., et al. (2021). Stratigraphic relationships in Jezero crater, Mars: Constrains on the timing of fluvial-lacustrine activity from orbital observations. *Journal of Geophysical Research: Planets*, *126*(7), e2021JE006840. https://doi.org/10.1029/2021JE006840

Holness, M. B. (2021). Cumulates and layered igneous rocks. In D. Alderton & S. A. Elias (Eds.), *Encyclopedia of geology* (2nd ed., pp. 99–112). Academic Press. https://doi.org/10.1016/B978-0-12-409548-9.12460-1

Horgan, B. H. N., Anderson, R. B., Dromart, G., Amador, E. S., & Rice, M. S. (2020). The mineral diversity of Jezero crater: Evidence for possible lacustrine carbonates on Mars. *Icarus*, *339*, 113526. https://doi.org/10.1016/j.icarus.2019.113526

Horgan, B. H. N., Udry, A., Rice, M. S., Alwmark, S., Amundsen, H. E., Bell, J. F. III, et al. (2023). Mineralogy, morphology, and emplacement history of the Máaz formation on the Jezero crater floor from orbital and rover observations. *Journal of Geophysical Research: Planets*. https://doi.org/10.1002/essoar.10512674.1

Johnson, J. R., Achilles, C., Bell, J. F., Bender, S., Cloutis, E., Ehlmann, B., et al. (2017). Visible/near-infrared spectral diversity from in situ observations of the Bagnold Dune Field sands in Gale Crater, Mars. *Journal of Geophysical Research: Planets*, *122*(12), 2655–2684. https://doi.org/10.1002/2016JE005187

Kelemen, P. B., Matter, J. M., de Obeso, J. C., Leong, J. A., Templeton, A., Ellison, E. T., et al. (2021). Initial results from the Oman Drilling Project Multi-Borehole Observatory: Petrogenesis and ongoing alteration of mantle peridotite in the weathering horizon. *Journal of Geophysical Research: Solid Earth*, *126*, e2021JB022729. https://doi.org/10.1029/2021JB022729

Klima, R. L., Dyar, M. D., & Pieters, C. M. (2011). Near-infrared spectra of clinopyroxenes: Effects of calcium content and crystal structure. *Meteoritics & Planetary Sciences*, *46*(3), 379–395. https://doi.org/10.1111/j.1945-5100.2010.01158.x

Kremer, C. H., Mustard, J. F., & Bramble, M. S. (2019). A widespread olivine-rich ash deposit on Mars. *Geology*, *47*(7), 677–681. https://doi.org/10.1130/G45563.1

Kuebler, K. E., Jolliff, B. L., Wang, A., & Haskin, L. A. (2006). Extracting olivine (Fo–Fa) compositions from Raman spectral peak positions. *Geochimica et Cosmochimica Acta*, *70*(24), 6201–6222. https://doi.org/10.1016/j.gca.2006.07.035

Lamadrid, H., Rimstidt, J., Schwarzenbach, E., Klein, F., Ulrich, S., Dolocan, A., & Bodnar, R. J. (2017). Effect of water activity on rates of serpentinization of olivine. *Nature Communications*, *8*(1), 16107. https://doi.org/10.1038/ncomms16107

Lapotre, M. G. A., Ehlmann, B. L., Minson, S. E., Arvidson, R. E., Ayoub, F., Fraeman, A. A., et al. (2017). Compositional variations in sands of the Bagnold Dunes, Gale crater, Mars, from visible-shortwave infrared spectroscopy and comparison with ground truth from the Curiosity rover. *Journal of Geophysical Research: Planets*, *122*(12), 2489–2509. https://doi.org/10.1002/2016JE005133

Lasue, J., Cousin, A., Meslin, P. Y., Mangold, N., Wiens, R. C., Berger, G., et al. (2018). Martian eolian dust probed by ChemCam. *Geophysical Research Letters*, *45*(20), 10–968. https://doi.org/10.1029/2018GL079210

Lentz, R. C. F., McCoy, T. J., Collins, L. E., Corrigan, C. M., Benedix, G. K., Taylor, G. J., & Harvey, R. P. (2011). Theo's flow, Ontario, Canada: A terrestrial analog for the Martian nakhlite meteorites. In W. Brent Garry & J. E. Bleacher (Eds.), *Analogs for planetary exploration* (Vol. 483). https://doi.org/10.1130/2011.2483(17)

Liu, Y., Tice, M. M., Schmidt, M. E., Treiman, A. H., Kizovski, T. V., Hurowitz, J. A., et al. (2022). An olivine cumulate outcrop on the floor of Jezero crater, Mars. *Science*, *377*(6614), 1513–1519. https://doi.org/10.1126/science.abo2756

Madariaga, J. M., Aramendia, J., Arana, G., Gomez-Nubla, L., Fdez-Ortiz de Vallejuelo, S., Garcia-Florentino, C., et al. (2022). Homogeneity assessment of the SuperCam calibration targets. *Analytica Chimica Acta*, *1209*, 339837. https://doi.org/10.1016/j.aca.2022.339837

Maki, J. M. (2020). Mars 2020 navigation cameras bundle, mosaic products [Dataset]. NASA Planetary Data System. https://doi.org/10.17189/0SXN-ZB41

Mandon, L., Quantin-Nataf, C., Royer, C., Beck, P., Fouchet, T., Johnson, J. R., et al. (2022). Reflectance of Jezero crater floor: 2. Mineralogical interpretations. *Journal of Geophysical Research: Planets*, e2022JE007450. https://doi.org/10.1029/2022JE007450

Mandon, L., Quantin-Nataf, C., Thollot, P., Mangold, N., Lozac'h, L., Dromart, G., et al. (2020). Refining the age, emplacement and alteration scenarios of the olivine-rich unit in the Nili Fossae region, Mars. *Icarus*, *336*, 113436. https://doi.org/10.1016/j.icarus.2019.113436

Mangold, N., Gupta, S., Gasnault, O., Dromart, G., Tarnas, J. D., Sholes, S. F., et al. (2021). Perseverance rover reveals an ancient delta-lake system and flood deposits at Jezero crater, Mars. *Science*, *374*(6568), 711–717. https://doi.org/10.1126/science.abl4051

Manrique, J. A., Lopez-Reyes, G., Cousin, A., Rull, F., Maurice, S., Wiens, R. C., et al. (2020). SuperCam calibration targets: Design and development. *Space Science Reviews*, *216*(8), 138. https://doi.org/10.1007/s11214-020-00764-w

Matzen, A. K., Woodland, A., Beckett, J. R., & Wood, B. J. (2022). Oxidation state of iron and Fe-Mg partitioning between olivine and basaltic martian melts. *American Mineralogist*, *107*(7), 1442–1452. https://doi.org/10.2138/am-2021-7682

Maurice, S., Clegg, S. M., Wiens, R. C., Gasnault, O., Rapin, W., Forni, O., et al. (2016). ChemCam activities and discoveries during the nominal mission of the Mars Science Laboratory in Gale crater, Mars. *Journal of Analytical Atomic Spectrometry*, *31*(4), 863–889. https://doi.org/10.1039/C5JA00417A

Maurice, S., Wiens, R. C., Bernardi, P., Caïs, P., Robinson, S., Nelson, T., et al. (2021). The SuperCam instrument suite on the Mars 2020 rover: Science objectives and mast-unit description. *Space Science Reviews*, *217*(3), 47. https://doi.org/10.1007/s11214-021-00807-w

Maurice, S., Wiens, R. C., Saccoccio, M., Barraclough, B., Gasnault, O., Forni, O., et al. (2012). The ChemCam instrument suite on the Mars Science Laboratory (MSL) rover: Science objectives and Mast unit description. *Space Science Reviews*, *170*(1–4), 95–166. https://doi.org/10.1007/s11214-012-9912-2

McCubbin, F. M., Elardo, S. M., Shearer, C. K., Jr., Smirnov, A., Hauri, E. H., & Draper, D. S. (2013). A petrogenetic model for the co-magmatic origin of chassignites and nakhlites: Inferences from chlorine-rich minerals, petrology, and geochemistry. *Meteoritics & Planetary Sciences*, *48*(5), 819–853. https://doi.org/10.1111/maps.12095

McSween, H. Y., Ruff, S. W., Morris, R. V., Bell, J. F., III, Herkenhoff, K., Gellert, R., et al. (2006). Alkaline volcanic rocks from the Columbia Hills, Gusev crater, Mars. *Journal of Geophysical Research*, *111*(E9), E09S91. https://doi.org/10.1029/2006JE002698

McSween, H. Y., Ruff, S. W., Morris, R. V., Gellert, R., Klingelhöfer, G., Christensen, P. R., et al. (2008). Mineralogy of volcanic rocks in Gusev crater, Mars: Reconciling mossbauer, Alpha Particle X-ray spectrometer, and miniature thermal emission spectrometer spectra. *Journal of Geophysical Research*, *113*(E6), E06S04. https://doi.org/10.1029/2007JE002970

Montagnac, G., Dromart, G., Beck, P., Mercier, B., Reynard, B., Cousin, A., et al. (2018). Spark plasma sintering preparation of reference targets for field spectroscopy on Mars. *Journal of Raman Spectroscopy*, *49*(9), 1419–1425. https://doi.org/10.1002/jrs.5406

Montserrat, F., Renforth, P., Hartmann, J., Leermakers, M., Knops, P., & Meysman, F. J. (2017). Olivine dissolution in seawater: Implications for CO_2 sequestration through enhanced weathering in coastal environments. *Environmental Science & Technology*, *51*(7), 3960–3972. https://doi.org/10.1021/acs.est.6b05942

Morris, R. V., Klingelhöfer, G., Schröder, C., Rodionov, D. S., Yen, A., Ming, D. W., et al. (2006). Mössbauer mineralogy of rock, soil, and dust at Meridiani Planum, Mars: Opportunity's journey across sulfate-rich outcrop, basaltic sand and dust, and hematite lag deposits. *Journal of Geophysical Research*, *111*(E12), E12S15. https://doi.org/10.1029/2006JE002791

Morrison, S. M., Downs, R. T., Blake, D. F., Vaniman, D. T., Ming, D. W., Hazen, R. M., et al. (2018). Crystal chemistry of martian minerals from bradbury landing through naukluft plateau, Gale crater, Mars. *American Mineralogist*, *103*(6), 857–871. https://doi.org/10.2138/am-2018-6124

Mustard, J. F., Ehlmann, B. L., Murchie, S. L., Poulet, F., Mangold, N., Head, J. W., et al. (2009). Composition, morphology, and stratigraphy of noachian crust around the Isidis basin. *Journal of Geophysical Research*, *114*(E2), E00D12. https://doi.org/10.1029/2009JE003349

Mustard, J. F., Poulet, F., Gendrin, A., Bibring, J.-P., Langevin, Y., Gondet, B., et al. (2005). Olivine and pyroxene diversity in the crust of Mars. *Science*, *307*(5715), 1594–1597. https://doi.org/10.1126/science.1109098

Mustard, J. F., Poulet, F., Head, J. W., Mangold, N., Bibring, J.-P., Pelkey, S. M., et al. (2007). Mineralogy of Nili Fossae region with OMEGA/Mars express data: 1. Ancient impact melt in the Isidis basin and implications for the transition from the noachian to hesperian. *Journal of Geophysical Research*, *112*(E8), E08S03. https://doi.org/10.1029/2006JE002834

O'Driscoll, B., Emeleus, C. H., Donaldson, C. H., & Daly, J. S. (2010). Cr-Spinel seam petrogenesis in the Rum layered suite, NW Scotland: Cumulate assimilation and *in situ* crystallization in a deforming crystal mush. *Journal of Petrology*, *51*(6), 1171–1201. https://doi.org/10.1093/petrology/egq013

Ody, A., Poulet, F., Bibring, J.-P., Loizeau, D., Carter, J., Gondet, B., & Langevin, Y. (2013). Global investigation of olivine on Mars: Insights into crust and mantle compositions. *Journal of Geophysical Research: Planets*, *118*(2), 234–262. https://doi.org/10.1029/2012JE004149

Palumbo, A. M., & Head, J. W. (2018). Early Mars climate history: Characterizing a "Warm and Wet" martian climate with a 3-D global climate model and testing geological predictions. *Geophysical Research Letters*, *45*(19). https://doi.org/10.1029/2018GL079767

Papike, J. J., Karner, J. M., Shearer, C. K., & Burger, P. V. (2009). Silicate mineralogy of martian meteorites. *Geochimica et Cosmochimica Acta*, *73*(24), 7443–7485. https://doi.org/10.1016/j.gca.2009.09.008

Payré, V., Fabre, C., Cousin, A., Sautter, V., Wiens, R. C., Forni, O., et al. (2017). Alkali trace elements in Gale crater, Mars, with ChemCam: Calibration update and geological implications. *Journal of Geophysical Research: Planets*, *122*(3), 650–679. https://doi.org/10.1002/2016JE005201

Peslier, A. H., Luhr, J. F., & Post, J. (2002). Low water contents in pyroxenes from spinel-peridotites of the oxidized, sub-arc mantle wedge. *Earth and Planetary Science Letters*, *201*, 69–86. https://doi.org/10.1016/S0012-821X(02)00663-5

Poulet, F., Mangold, N., Platevoet, B., Bardintzeff, J.-M., Sautter, V., Mustard, J. F., et al. (2009). Quantitative compositional analysis of martian mafic regions using the MEx/OMEGA reflectance data: 2. Petrological implications. *Icarus*, *201*(1), 84–101. https://doi.org/10.1016/j.icarus.2008.12.042

Poulet, F., Royer, C., Beck, P., Mandon, L., Quantin-Nataf, C., Johnson, J. R., et al. (2022). Modal mineralogy of Séitah unit in Jezero crater (Mars) retrieved from nonlinear unmixing analyses of IRS/SuperCam. In *53rd Lunar and Planetary Science Conference 2022* (p. 2032). Retrieved from https://www.hou.usra.edu/meetings/lpsc2022/pdf/2032.pdf

Puddu, C., Alvaro, J. J., Carrera, N., & Casas, J. M. (2019). Deciphering the sardic (Ordovician) and Variscan deformations in the eastern pyrenees, SW Europe. *Journal of the Geological Society*, *176*(6), 1191–1206. https://doi.org/10.1144/jgs2019-057

Pyke, D. R., Naldrett, A. J., & Eckstrand, O. R. (1973). Archean ultramafic flows in Munro township, Ontario. *GSA Bulletin*, *84*(3), 955–978. https://doi.org/10.1130/0016-7606(1973)84%3C955:AUFIMT%3E2.0.CO;2

Quantin-Nataf, C., Alwmark, S., Calef, F. J., Lasue, J., Kinch, K., Stack, K. M., et al. (2023). The complex exhumation history of Jezero crater floor unit and its implication for Mars sample return. *Journal of Geophysical Research: Planets*, *128*, e2022JE007628. https://doi.org/10.1029/2022JE007628

Rahib, R. R., Udry, A., Howarth, G. H., Gross, J., Paquet, M., Combs, L. M., et al. (2019). Mantle source to near-surface emplacement of enriched and intermediate poikilitic shergottites in Mars. *Geochimica et Cosmochimica Acta*, *266*, 463–496. https://doi.org/10.1016/j.gca.2019.07.034

Rapin, W., Meslin, P.-Y., Maurice, S., Wiens, R. C., Laporte, D., Chauviré, B., et al. (2017). Quantification of water content by LIBS on Mars. *Spectrochimica Acta Part B: Atomic Spectroscopy*, *130*, 82–100. https://doi.org/10.1016/j.sab.2017.02.007

Rogers, A. D., Warner, N. H., Golombek, M. P., Head, J. W., III, & Cowart, J. C. (2018). Areally extensive surface bedrock exposures on Mars: Many are clastic rocks, not lavas. *Geophysical Research Letters*, *45*(4), 1767–1777. https://doi.org/10.1002/2018GL077030

Royer, C., Fouchet, T., Mandon, L., Montmessin, F., Poulet, F., Forni, O., et al. (2023). Reflectance of Jezero crater Floor: 1. Data processing and calibration of the infrared spectrometer (IRS) on SuperCam. *Journal of Geophysical Research: Planets*, *128*(1), e2022JE007481. https://doi.org/10.1029/2022JE007450

Salvatore, M. R., Goudge, T. A., Bramble, M. S., Edwards, C. S., Bandfield, J. L., Amador, E. S., et al. (2018). Bulk mineralogy of the NE Syrtis and Jezero crater regions of Mars derived through thermal infrared spectral analyses. *Icarus*, *301*, 76–96. https://doi.org/10.1016/j.icarus.2017.09.019

Santos, A. R., Agee, C. B., McCubbin, F. M., Shearer, C. K., Burger, P. V., Tartèse, R., & Anand, M. (2015). Petrology of igneous clasts in Northwest Africa 7034: Implications for the petrologic diversity of the martian crust. *Geochimica et Cosmochimica Acta*, *157*, 56–85. https://doi.org/10.1016/j.gca.2015.02.023

Sautter, V., Toplis, M., Wiens, R., Cousin, A., Fabre, C., Gasnault, O., et al. (2015). *In situ* evidence for continental crust on early Mars. *Nature Geoscience*, *8*, 605–609. https://doi.org/10.1038/ngeo2474

Scheller, E. L., Razzell Hollis, J., Cardarelli, E. L., Steele, A., Beegle, L. W., Bhartia, R., et al. (2022). Aqueous alteration processes in Jezero crater, Mars—Implications for organic geochemistry. *Science*, *378*(6624), 1105–1110. https://doi.org/10.1126/science.abo5204

Sherman, D. M., & Waite, T. D. (1985). Electronic spectra of Fe^{3+} oxides and oxide hydroxides in the near IR to near UV. *American Mineralogist*, *70*, 1262–1269.

Simon, J. J., Hickman-Lewis, K., Cohen, B. A., Mayhew, L. E., Shuster, D. L., Debaille, V., et al. (2023). Samples collected from the floor of Jezero Crater with the Mars 2020 perseverance rover. *Journal of Geophysical Research: Planets*, e2022JE007474. https://doi.org/10.1029/2022JE007474

Skok, J. R., Mustard, J. F., Murchie, S. L., Wyatt, M. B., & Ehlmann, B. L. (2010). Spectrally distinct ejecta in Syrtis Major, Mars: Evidence for environmental change at the Hesperian-Amazonian boundary. *Journal of Geophysical Research*, *115*, E00D14. https://doi.org/10.1029/2009JE003338

Stack, K. M., Williams, N. R., Calef, F., Sun, V. Z., Williford, K. H., Farley, K. A., et al. (2020). Photogeologic map of the perseverance rover field site in Jezero crater constructed by the Mars 2020 science team. *Space Science Reviews*, *216*(8), 127. https://doi.org/10.1007/s11214-020-00739-x

Sun, V., Hand, K. P., Stack, K. M., Farley, K. A., Simon, J. I., Newman, C., et al. (2023). Overview and results from the Mars 2020 perseverance rover's first science campaign on the Jezero Crater Floor. *Journal of Geophysical Research: Planets*, e2022JE007613. https://doi.org/10.1029/2022je007613

Tarnas, J. D., Stack, K. M., Parente, M., Koeppel, A. H. D., Mustard, J. F., Moore, K. R., et al. (2021). Characteristics, origins, and biosignature preservation potential of carbonate-bearing rocks within and outside of Jezero crater. *Journal of Geophysical Research: Planets*, *126*(11), e2021JE006898. https://doi.org/10.1029/2021JE006898

Thybo, H., & Artemieva, I. M. (2013). Moho and magmatic underplating in continental lithosphere. *Tectonophysics*, *609*, 605–619. https://doi.org/10.1016/j.tecto.2013.05.032

Tice, M. M., Hurowitz, J. A., Allwood, A. C., Jones, M. W. M., Orenstein, B. J., Davidoff, S., et al. (2022). Alteration history of Séítah formation rocks inferred by PIXL x-ray fluorescence, x-ray diffraction, and multispectral imaging on Mars. *Science Advances*, *8*(47), eabp9084. https://doi.org/10.1126/sciadv.abp9084

Tornabene, L. L., Moersch, J. E., McSween, H. Y., Hamilton, V. E., Piatek, J. L., & Christensen, P. R. (2008). Surface and crater-exposed lithologic units of the Isidis Basin as mapped by coanalysis of THEMIS and TES derived data products. *Journal of Geophysical Research*, *113*(E10), E10001. https://doi.org/10.1029/2007JE002988

Treiman, A. H. (2005). The nakhlite meteorites: Augite-rich igneous rocks from Mars. *Chemie Der Erde-Geochemistry*, *65*(3), 203–270. https://doi.org/10.1016/j.chemer.2005.01.004

Treiman, A. H., & Filiberto, J. (2015). Geochemical diversity of shergottite basalts: Mixing and fractionation, and their relation to Mars surface basalts. *Meteoritics & Planetary Sciences*, *50*(4), 632–648. https://doi.org/10.1111/maps.12363

Udry, A., & Day, J. M. D. (2018). 1.34 billion-year-old magmatism on Mars evaluated from the co-genetic nakhlite and chassignite meteorites. *Geochimica et Cosmochimica Acta*, *238*, 292–315. https://doi.org/10.1016/j.gca.2018.07.006

Udry, A., Howarth, G. H., Herd, C., Day, J. M. D., Lapen, T. J., & Filiberto, J. (2020). What martian meteorites reveal about the interior and surface of Mars. *Journal of Geophysical Research: Planets*, *55*(12). https://doi.org/10.1029/2020JE006523

Udry, A., Ostwald, A., Sautter, V., Cousin, A., Beyssac, O., Forni, O., et al. (2022). A Mars 2020 *perseverance* SuperCam perspective on the igneous nature of the Máaz formation at Jezero crater and link with Séítah, Mars. *Journal of Geophysical Research: Planets*, e2022JE007440. https://doi.org/10.1029/2022JE007440

Ulven, O. I., Beinlich, A., Hövelmann, J., Austrheim, H., & Jamtveit, B. (2017). Subarctic physicochemical weathering of serpentinized peridotite. *Earth and Planetary Science Letters*, *468*, 11–26. https://doi.org/10.1016/j.epsl.2017.03.030

Vaniman, D. T., Bish, D. L., Ming, D. W., Bristow, T. F., Morris, R. V., Blake, D. F., et al. (2014). Mineralogy of a mudstone at Yellowknife Bay, Gale crater, Mars. *Science*, *343*(6169). https://doi.org/10.1126/science.1243480

Wiens, R. C., & Maurice, S. (2021). Mars 2020 SuperCam bundle [Dataset]. NASA Planetary Data System. https://doi.org/10.17189/1522646

Wiens, R. C., Maurice, S., Barraclough, B., Saccocio, M., Barkley, W. C., Bel, J. F., et al. (2012). The ChemCam instrument suite on the Mars Science Laboratory (MSL) rover: Body unit and combined system tests. *Space Science Reviews*, *170*(1–4), 167–227. https://doi.org/10.1007/s11214-012-9902-4

Wiens, R. C., Maurice, S., Robinson, S. H., Nelson, A. E., Cais, P., Bernardi, P., et al. (2021). The SuperCam instrument suite on the NASA Mars 2020 rover: Body unit and combined system tests. *Space Science Reviews*, *217*(1), 4. https://doi.org/10.1007/s11214-020-00777-5

Wiens, R. C., Udry, A., Beyssac, O., Quantin-Nataf, C., Mangold, N., Cousin, A., et al. (2022). Compositionally and density stratified igneous terrain in Jezero crater, Mars. *Science Advances*, *8*(34), eabo3399. https://doi.org/10.1126/sciadv.abo3399

Wittmann, A., Korotev, R. L., Jolliff, B. L., Irving, A. J., Moser, D. E., Barker, I., & Rumble, D. (2015). Petrography and composition of Martian regolith breccia meteorite Northwest Africa 7475. *Meteoritics & Planetary Sciences*, *50*(2), 326–352. https://doi.org/10.1111/maps.12425